

Reactive Sputtered Wide-Bandgap p-Type Semiconducting Spinel AB_2O_4 and Delafossite ABO_2 Thin Films for “Transparent Electronics”

A.N. Banerjee and K.K. Chattopadhyay

12.1 Introduction

Reactive sputtering is one of the most widely used techniques for preparing compound thin films (such as oxides, nitrides, carbides, etc.) by sputtering metal targets in an active gas atmosphere ($Ar + O_2/N_2/CH_4$, etc.) [1–4]. In this chapter, we have discussed, in details, the formation of spinel and delafossite materials of the form AB_2O_4 and ABO_2 (A and B may be monovalent, divalent, trivalent, or tetravalent cations, depending on the crystal structure, described later) by reactive sputtering technique. Specially, wide bandgap, p-type semiconducting, and transparent oxide materials with delafossite and spinel structure, having interesting applications in “Transparent Electronics,” have been discussed in details. In Sects. 12.2–12.5, a detailed review on the structural, optical, and electrical properties of these p-type transparent conducting oxides (p-TCOs), deposited by reactive sputtering technique, has been presented and the origin of p-type conductivity of these materials has been discussed with considerable attention. Most of the results presented in these sections are reported by various authors working on this field. In Sect. 12.6, synthesis and electro-optical characterization of one of the very important delafossite, p-type semiconducting, and wide-bandgap material, such as $CuAlO_2$, produced by our group via reactive sputtering technique, have been discussed in details. Detailed discussions on spinel- and delafossite-structured material can be found in various literatures [5–14]. Also, detailed reviews on the p-TCO materials have been published by us and others [15–17], which cover the syntheses and properties of a range of p-TCO materials reported so far.

12.2 Spinel and Delafossite Material

12.2.1 Spinel Materials

Spinel structure is an important ternary metal oxide crystal structure shown in Fig. 12.1. The spinel structure (sometimes called *garnet structure*) is named after the mineral spinel (MgAl_2O_4). The oxide may be written in the form of $\text{A}^{\text{II}}\text{B}_2^{\text{III}}\text{O}_4$ (called *2-3 spinel*) or $\text{A}^{\text{IV}}\text{B}_2^{\text{II}}\text{O}_4$ (called *4-2 spinel*), where $\text{A}^{\text{II}+}$ and $\text{A}^{\text{IV}+}$ are the divalent and tetravalent cations of type-I and $\text{B}^{\text{III}+}$ and $\text{B}^{\text{II}+}$ are the trivalent and divalent cations of type-II, respectively. In “normal” spinel structure, 12.5% of the tetrahedral sites and 50% of the octahedral sites of this structure are occupied by A and B cations, respectively, and there are 32 O^{2-} ions in a unit cell. On the other hand, in the “inverse” spinel structure, the site occupancies of two types of cations are swapped. Also, there are some intermediate phases with the formula $(\text{A}_{1-x}\text{B}_x)[\text{A}_x\text{B}_{2-x}]\text{O}_4$ also exist. Here, cations in the square brackets occupy the octahedral sites and cations in the parentheses occupy the tetrahedral sites.

The spinel crystal structure has a closed-packed fcc array of anions, with space group $\text{Fd}\bar{3}\text{m}$ or O_h^7 . When an fcc cubic cell of edge a and occupied by A atoms is subdivided into eight octants with edge $a/2$, four of the octants are occupied by AO_4 clusters and the other four of the octants are occupied by B_4O_4 clusters. The A atom is centered on the AO_4 tetrahedron cluster with four nearest-neighbor O atoms, while the B atom is at the corner of the octahedron cluster with six nearest-neighbor O atoms. The O atoms are positioned in the same way in all octants with one A atom and three B atoms as their nearest neighbors. In an inverse spinel structure, the tetrahedral sites are occupied by B atoms while the octahedral sites are occupied by equal numbers of A and B atoms.

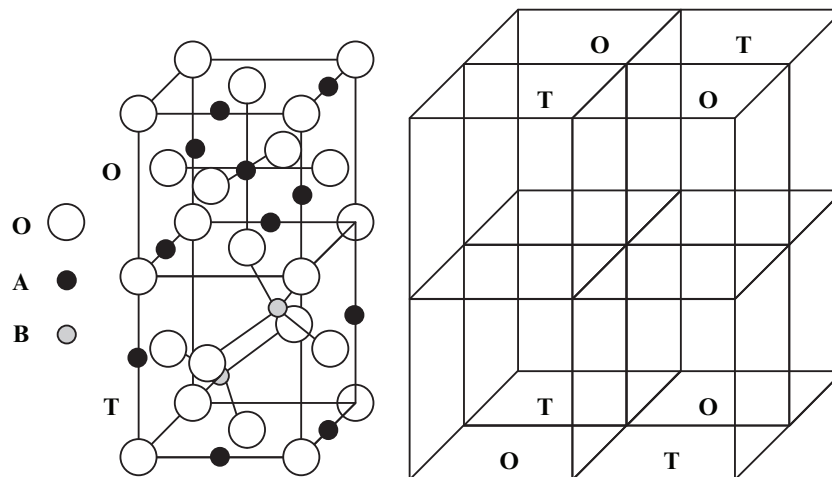


Fig. 12.1. Spinel crystal structure

The spinel structure is very flexible with respect to the cations it can incorporate. There are over 100 known compounds with this type of crystal structure. In particular, the two cations (say, A and B) can mix, so that the composition with respect to one unit cell can become $(A_8)(B_{16})O_{32}$, or $A_8(A_8B_8)O_{32} = A(AB)O_4$ in regular chemical spelling, or $(A_{8/3}B_{16/3})(A_{16/3}B_{32/3})O_{32}$, and so on, with the atoms in the brackets occupying the respective site at random. Examples of ternary metal oxides with 2–3 spinel structure are $MgAl_2O_4$, $MgGa_2O_4$, $ZnAl_2O_4$, $ZnGa_2O_4$, $ZnIn_2O_4$, $ZnIr_2O_4$, $ZnCo_2O_4$, $ZnRh_2O_4$, $CdAl_2O_4$, $CdGa_2O_4$, $CuAl_2O_4$, $CuMn_2O_4$, $NiCo_2O_4$, $NiFe_2O_4$, $NiCr_2O_4$, $LiTi_2O_4$, $LiMn_2O_4$, $LiAl_2O_4$, $CdRh_2O_4$, $FeCr_2O_4$, FeV_2O_4 , $MgCr_2O_4$, $ZnFe_2O_4$, $ZnMn_2O_4$, $FeAl_2O_4$, $HgCr_2O_4$, etc. Similarly, examples of ternary metal oxides with 4–2 spinel structure are $MoAg_2O_4$, $MnFe_2O_4$, $GeCo_2O_4$, $GeMg_2O_4$, $GeZn_2O_4$, $GeCd_2O_4$, $NbZn_2O_4$, $TiFe_2O_4$, $SiMg_2O_4$, $SiZn_2O_4$, $SiCd_2O_4$, etc. It is noteworthy that some of the binary metal oxides such as Fe_3O_4 also exhibit spinel crystal structure. But in this case, the A^{II+} and B^{III+} cations are same element (Fe) but exhibit both +2 and +3 valence states (as $Fe^{+2}OFe_2^{+3}O_3 = Fe^{+2}Fe_2^{+3}O_4$), respectively. Also, it is worthwhile in mentioning that there are some reports on quaternary oxides having spinel structure, such as $LiFeTiO_4$ [18], $Ca_4Fe_{1.5}Al_{17.67}O_{32}$ [19], $Mn_{(2-x)}CO_{2x}Ni_{(1-x)}O_4$ [20] $FeCoCrO_4$ ($Fe^{+3}Co^{+2}Cr^{+3}O_4$ or $Fe^{+3}Co^{+3}Cr^{+2}O_4$ or $Fe^{+2}Co^{+3}Cr^{+3}O_4$) [21], etc. Besides oxides, there are some ternary nonoxides exist which are having spinel structure, such as $AgAl_2S_4$, $CaIn_2S_4$, $CuTi_2S_4$, $CuIr_2S_4$, $ZnCr_2S_4$, $FeIn_2S_4$, $CuCr_2Te_4$, $CuCr_2Se_4$, $CdCr_2Se_4$, Li_2NiF_4 [22, 23], etc. $MgAlON$ [24] is an oxynitride material having spinel structure. Example of binary nonoxide spinel material includes $\gamma\text{-}Ge_3N_4$, Co_3O_4 (sometimes written as $CoCo_2O_4$), etc. [25, 26]. Lastly, examples of inverse spinel include $SnMg_2O_4$, $CdIn_2O_4$, $MgIn_2O_4$, $CuFe_2O_4$, $CuCr_2O_4$, $SnCd_2O_4$, $SnZn_2O_4$, $LiCuVO_4$, $LiNiVO_4$, $MnIn_2S_4$, etc. [27–30].

As far as applications of spinel materials are concerned, many of the spinels have interesting electronic and magnetic properties [31] and, therefore, suitable for various technological applications, which include superconductors [32, 33], magnetic core materials [34, 35], high-frequency devices [36], cathode material for commercial lithium secondary batteries [18, 36], magnetic semiconductors for spintronics applications [37], gas sensors [26], etc. Since many of the spinels are common minerals, therefore, in addition to the materials science studies, some of the spinel materials also have great importance geophysical studies [38–41]. Also the study of large bandgap spinels (e.g., $MgAl_2O_4$, $SnCd_2O_4$, $SnZn_2O_4$, $CdIn_2O_4$, etc.), with high electroconductivity, opens many interesting applications in optoelectronic device technology. These wide-bandgap materials are transparent in the visible and infrared regions and therefore have important applications in transparent electrodes, flat panel displays, infrared windows, missile domes, thin film solar cells, low-energy architectural window coatings, and many such applications [27, 42–50]. Also, CdTe solar cells using Cd_2SnO_4/Zn_2SnO_4 as transparent conductor layers have achieved the highest cell efficiency

known for this system [51]. And lastly, within the class of transparent spinel oxides, p-type semiconducting, wide bandgap, and transparent spinel oxides (e.g., NiCo_2O_4 , ZnIr_2O_4 , ZnRh_2O_4 , etc. [52–55]) have recently generated great interest in the field of optoelectronic device technology for the possible applications in “Transparent Electronics” [56]. Therefore, these reports have rekindled the interest to study the fundamental physics in spinel oxide systems.

12.2.2 Delafossite Materials

Delafossite structure is another important crystal structure for ternary metal oxides. The oxides are generally of the form of $\text{A}^{\text{I}}\text{B}^{\text{III}}\text{O}_2$, where A^{I} represents the monovalent cation and B^{III} represents the trivalent cation. The structure, as shown in Fig. 12.2, consists of an alternative stacking of A^{I} and layers of nominal $\text{B}^{\text{III}}\text{O}_2$ composition consisting $\text{B}^{\text{III}}\text{O}_6$ octahedra sharing edges. Each A^{I} atom is linearly coordinated with two oxygen atoms to form an $\text{O}-\text{A}^{\text{I}}-\text{O}$ dumbbell unit placed parallel to the c -axis. O atoms of $\text{O}-\text{A}^{\text{I}}-\text{O}$ dumbbell link all A^{I} layers with the $\text{B}^{\text{III}}\text{O}_2$ layers [12–14]. On the other hand, each oxide ion in the $\text{B}^{\text{III}}\text{O}_2$ layer forms a “pseudotetrahedral coordination ($\text{B}_3^{\text{III}}\text{A}^{\text{I}}\text{O}$)” with the neighboring B^{III} and A^{I} ions. Ternary metal oxides having this type of crystal structure include PdCoO_2 , PtCoO_2 , PtCrO_2 , PtRhO_2 , CuAlO_2 , CuFeO_2 , CuGaO_2 , CuScO_2 , CuYO_2 , CuCrO_2 , CuInO_2 , CuRhO_2 , CuLaO_2 , CuPrO_2 , CuNdO_2 , CuSmO_2 , CuEuO_2 , AgInO_2 , AgScO_2 , AgCrO_2 , AgGaO_2 , AgCoO_2 , AgFeO_2 , AgRhO_2 , AgAlO_2 , etc. Quaternary oxides with delafossite structure include $\text{AgNi}_{1-x}\text{Sb}_x\text{O}_2$, $\text{AgZn}_{1-x}\text{Sb}_x\text{O}_2$, $\text{CuGa}_{1-x}\text{Fe}_x\text{O}_2$, $\text{CuIn}_{1-x}\text{Ca}_x\text{O}_2$, $\text{AgIn}_{1-x}\text{Mg}_x\text{O}_2$, $\text{CuCo}_{1-x}\text{Ti}_x\text{O}_2$, $\text{CuNi}_{1-x}\text{Ti}_x\text{O}_2$, $\text{CuCu}_{1-x}\text{Ti}_x\text{O}_2$, $\text{CuNi}_{1-x}\text{Sn}_x\text{O}_2$, $\text{CuFe}_{1-x}\text{V}_x\text{O}_2$, $\text{AgNi}_{1-x}\text{Ti}_x\text{O}_2$, etc. [12–17].

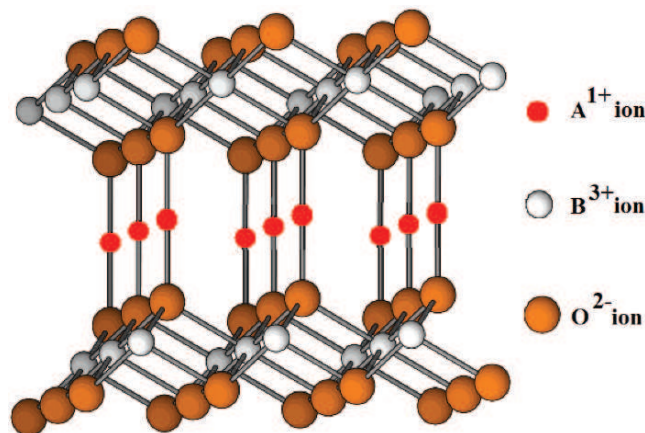


Fig. 12.2. Delafossite crystal structure

Table 12.1. Various properties of spinel and delafossite crystal structures

Structure	Stoichiometry	Space group	Coordination no. (CN)/geometry	Representative oxides
Spinel	AB_2O_4	$Fd\bar{3}m$	A: CN = 4/tetrahedral coordination B: CN = 6/octahedral coordination O: CN = 4/distorted tetrahedral coordination	$NiCo_2O_4$, $MgAl_2O_4$, $MgGa_2O_4$, $ZnAl_2O_4$, $ZnGa_2O_4$, $ZnIn_2O_4$, $ZnIr_2O_4$, $ZnCo_2O_4$, $ZnRh_2O_4$, $CdAl_2O_4$, $CdGa_2O_4$, etc.
Delafossite	ABO_2	$R\bar{3}m$	A: CN = 4/square planer coordination B: CN = 6/octahedral coordination O: CN = 1A + 3B/tetrahedral coordination	$CuAlO_2$, $CuFeO_2$, $CuGaO_2$, $CuScO_2$, $CuYO_2$, $CuCrO_2$, $CuInO_2$, $AgInO_2$, $AgScO_2$, $AgCrO_2$, $AgGaO_2$, $PdCoO_2$, etc.

As far as applications of delafossite materials are concerned, these materials have potential applications in thermoelectric devices [57–62], field-emission displays (FEDs) [63], ozone sensors [64], photocatalytic hydrogen generators [65], magnetic semiconductors for spintronics [66], etc. But, as most of the delafossite materials are wide-bandgap transparent materials, therefore they have lots of applications in optoelectronics technology. Especially, as most of these materials are p-type semiconducting transparent oxides, they have potential applications in “Invisible” or “Transparent Electronics” [15–17, 56]. Detailed review of various p-TCOs with spinel and delafossite structure is discussed in subsequent sections (Table 12.1).

12.3 p-Type Transparent Conducting Oxides Based on Spinel and Delafossite Structure

12.3.1 Introduction to Transparent Conducting Oxides

Transparent conducting oxides (TCOs) are very important materials that create great interest within materials scientists for its overwhelming applications in the field of optoelectronic device technology. The characteristics of such films are high room temperature electrical conductivity ($\sim 10^3 \text{ S cm}^{-1}$ or more) and high optical transparency (more than 80%) in the visible region. TCOs are well known and widely used for a long time in optoelectronics industries as well as in research fields. After the first report of transparent

conducting cadmium oxide (CdO) thin film by Badekar [67] in 1907, extensive works have been done in the field of TCO technology to prepare new types of TCOs with wide ranging applications [68–78]. Technologically, these TCOs are being used extensively in various fields, which include solar cells, flat panel displays (FPDs), low-emissivity (“low-*e*”) windows, electromagnetic shielding of cathode-ray tubes in video display terminals, electrochromic (EC) materials in rear-view mirrors of automobiles, EC-windows for privacy (so-called smart windows), oven windows, touch-sensitive control panels, defrosting windows in refrigerators and airplanes, invisible security circuits, gas sensors, biosensors, organic light-emitting diodes (OLED), polymer light-emitting diodes (PLED), antistatic coatings, cold heat mirrors, etc. [67–70, 74, 75, 79–90]. Also some new applications of TCOs have been proposed recently such as holographic recording medium, high-refractive index waveguide overlays for sensors and telecommunication applications, write-once read-many-times memory chips (WORM), electronic ink, etc. [91–94]. And lastly, the low-temperature deposition of TCOs onto poly(ethylene terephthalate) (PET), polyamides, and other polymer substrates in roll-coating processes for touch-screen and infrared reflector applications is the recent challenges for the TCO industries [95–97].

Possibility of the aforementioned novel applications of TCOs is based on the fact that the electronic bandgap of a TCO is higher than 3.1 eV (corresponding to the energy of a 400 nm blue photon). So visible photons (having energy between 2.1 and 3.1 eV) cannot excite electrons from valence band (VB) to the conduction band (CB) and hence are transmitted through it, whereas they have enough energy to excite electrons from donor level to CB (for n-type TCO) or holes from acceptor level to VB (for p-type TCO). And these acceptor or donor levels are created in the TCOs by introducing nonstoichiometry and/or appropriate dopants in a controlled manner. A schematic representation of the bandgap designing for transparent conductors is shown in Fig. 12.3.

12.3.2 Transparent Electronics

Although the TCOs have vast range of applications as mentioned above, very little work has been done on the active device fabrication using TCOs [98, 99]. This is because most of the aforementioned TCOs are n-type semiconductors. But the corresponding p-TCOs, which are essential for junctional devices, were surprisingly missing in thin film form for a long time, until in 1997, Kawazoe et al. [100] reported the p-type conductivity in a highly transparent thin film of copper aluminum oxide (CuAlO_{2+x}). This has opened up a new field in optoelectronic device technology, the so-called “Transparent Electronics” or “Invisible Electronics,” where a combination of the two types of TCOs in the form of a p–n junction could lead to a “functional” window, which transmits visible portion of solar radiation yet generates electricity by the absorption of UV part [56]. It must be mentioned here that the first report of semitransparent p-type conducting thin film of nickel oxide was published in 1993 by Sato

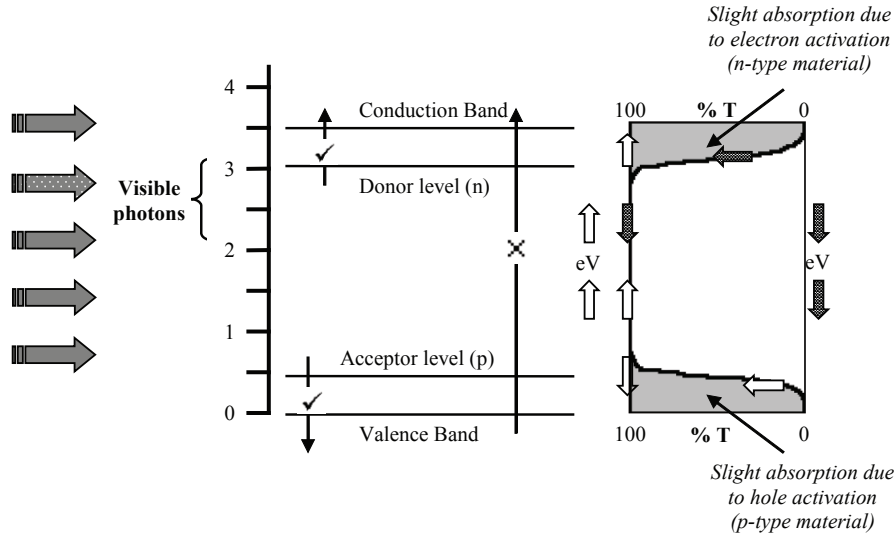


Fig. 12.3. Bandgap designing for transparent conductors. Visible photons (2.1–3.1 eV) do not have enough energy to excite electrons from valence band to conduction band, but have enough energy to excite holes (for p-type) from acceptor level to VB or electrons (for n-type) from donor level to CB (after [38]). Right-hand side shows the transmittance of the TCO with respect to incident radiation. The arrow “ \rightleftharpoons ” indicates the transmittance graph for a p-type TCO, where a slight absorption can be observed (indicated by *shaded part*) at low-energy region, due to the activation of holes from acceptor level to VB. Similarly, the arrow “ \Rightarrow ” indicates the same for n-type TCO, where slight absorption at low-energy region takes place due to electron activation from donor level to CB

et al. [101]. They observed only 40% transmittance of the NiO films in the visible region and when they tried to fabricate an all-TCO p–i–n diode of the form p-NiO/i-NiO/i-ZnO/n-ZnO, the visible transmittance further reduced to almost 20%. Although this low transmittance was not favorable for superior device applications, but still this report was an important milestone in the field of “Transparent Electronics” and in the development of TCO technology.

Now for diverse device applications, it is utmost important to prepare various new types of p-TCOs with superior optical and electrical characteristics, at least comparable to the existing, widely used n-TCOs, which are having transparency above 80% in the visible region and conductivity about $1,000 \text{ S cm}^{-1}$ or more. Intense works have been done for the last few years in this direction to fabricate new p-TCOs by various deposition techniques. Also, quite a number of works have been carried out for proper understanding of the structural, optical, and electrical characteristics of p-TCOs. As this is an emerging field in TCO technology, preparation of new materials as well as existing materials with new deposition techniques is the need of the hour.

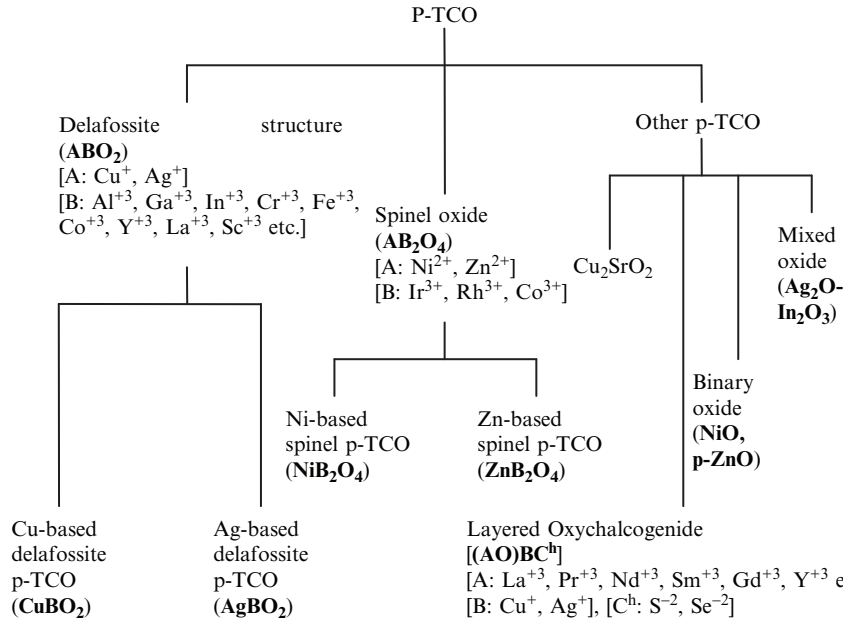


Fig. 12.4. Chart of various p-TCO materials reported so far. Here, the doped versions of Cu-based delafossite p-TCOs have been mentioned only

A chart of various p-TCO materials developed so far for potential applications in “Transparent Electronics” is furnished in Fig. 12.4.

12.3.3 p-TCO with Spinel Structure

Amongst various p-TCOs based on spinel structure, cobalt nickel oxide ($NiCo_2O_4$) is the first material reported to have p-type conductivity with reasonable visible transparency ($\sim 40-60\%$) [52], in thin film form. A variation in the conductivity is observed in this material with a change in the Ni:Co ratio and at Ni:Co = 1:2, the highest conductivity in these films was observed around $16.0 S cm^{-1}$. It has also been proposed by various authors that Ni^{+3} ions located on octahedral sites within the spinel lattice enhance the conductivity of the film [102]. Figure 12.5 shows the variation of resistivity of Ni–Co–O thin films with composition x ($=Co/\{Co + Ni\}$). Minimum resistivity obtained at $x = 0.67$. These films also showed good transparency in the infrared region, extending its application into infrared optics [52, 103].

Another group of p-type semiconducting transparent spinel oxides, based on Zn- (d^6) transition metals, is ZnB_2O_4 ($B = Co, Rh, Ir$) [54, 55], which shows optical bandgaps around 3 eV and electrical conductivity as high as $2.0 S cm^{-1}$. Figure 12.6 shows the electrical conductivity of $ZnRh_2O_4$ thin film and Fig. 12.7 shows the optical transparency of ZnB_2O_4 ($B = Co, Rh, Ir$) thin

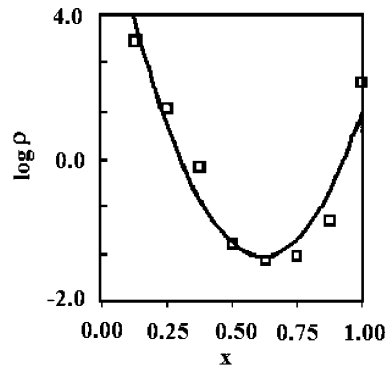


Fig. 12.5. Variation of resistivity of Ni-Co-O thin films with composition x ($= \text{Co}/\{\text{Co} + \text{Ni}\}$). Minimum resistivity obtained at $x = 0.67$ (after [53])

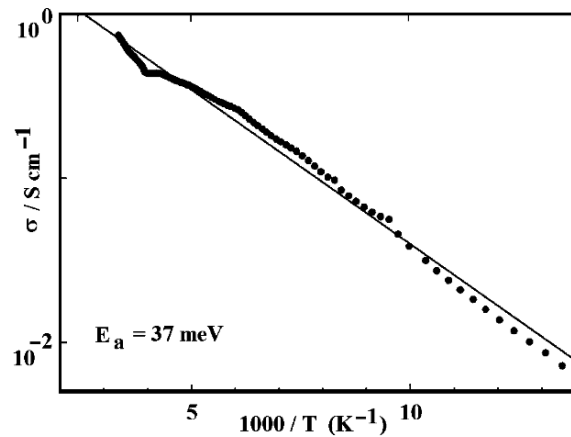


Fig. 12.6. Temperature variation of electrical conductivity of ZnRh_2O_4 thin film (after [55]). E_a is the activation energy, which is the minimum energy required to transfer an electron from donor level to CB (for n-type material) or holes from acceptor level to VB

films deposited on quartz substrates. Also Table 12.2 shows the optoelectrical properties of various spinel p-TCOs.

As far as deposition of spinel p-TCOs is concerned, Windisch and coauthors [52, 53, 103] used both physical and chemical techniques to prepare Ni-based spinel films (e.g., NiCo_2O_4). For chemical method, they have used spin-coating technique [53] with a precursor solution containing the respective metal nitrates and an organic complexant. Subsequent thermal annealing induced oxide formation during which the organic component was fully oxidized to gaseous products. On the other hand, physical deposition of NiCo_2O_4 involved radio frequency (RF) magnetron sputtering technique [52]. The target used was Ni-Co alloys with a RF power of 200 W. It has been

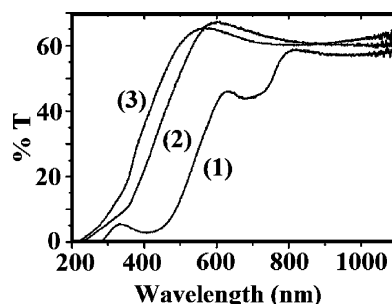


Fig. 12.7. Spectral variation of optical transmittance of (1) ZnCo₂O₄, (2) ZnRh₂O₄, and (3) ZnIr₂O₄ thin films (redrawn from [54] with permission)

observed that the quality of the RF sputtered film is better than that of solution-deposited film [53] and with increasing Ni concentration, the film showed enhanced electrical conductivity up to a value of $x = 0.67$. The film composition can be expressed as Ni_{1+x}Co_{2-x}O₄, and with $x = 0.5$, the film showed best electro-optical properties. Various deposition parameters of RF sputtered NiCo₂O₄ film are furnished in Table 12.3. The same group also used a “combinatorial” sputtering technique to deposit an array of films with varying film compositions with a single run under identical deposition conditions [103]. This special technique was used to study the effect of selected gas compositions on the deposited films. And, they have observed that the optimum conductivity from combinatorially deposited films containing equal parts of nickel and cobalt (i.e., Ni_{1.5}Co_{1.5}O₄) is achieved when sputtered in a gas mixture of 50% argon and 50% oxygen from oxide targets, with the best film conductivity of 375 S cm⁻¹ achieved using growth conditions that promote complete oxidation. For the deposition of Zn-based spinel p-TCO films (e.g., ZnRh₂O₄, ZnCo₂O₄, ZnIr₂O₄, etc.), Dekkers et al. [54] used pulsed laser deposition (PLD) technique from respective sintered targets. Various electro-optical properties of these films are furnished in Table 12.2. On the other hand, Mizoguchi and coauthors [55, 104] used RF sputtering technique to deposit crystalline as well as amorphous ZnRh₂O₄ thin films on silica glass substrates. They have used identical sputtering conditions for both crystalline and amorphous films but postannealing treatment was done on a-ZnRh₂O₄ films to get the crystalline phase of the film. Various deposition conditions of these films are furnished in Table 12.3.

As far as reactive sputtering of spinel p-TCOs is concerned, Kim and coauthors [37] used reactive magnetron cosputtering technique to deposit ZnCo₂O₄ thin film from metallic targets. Detailed discussions of the reactively sputtered spinel p-TCOs are furnished in later sections.

12.3.4 p-TCO with Delafossite Structure

Delafossite-structured oxides (ABO₂; A: monovalent cation, B: trivalent cation) can be divided into two groups: one having A-d¹⁰ (e.g., A = Cu, Ag)

Table 12.2. Optoelectrical properties of various spinel p-TCOs

Material	Deposition technique	Average film thickness (nm)	Transmittance (T) (%)	Direct bandgap ($E_{g\text{-direct}}$) (eV)	Room temp. conductivity (σ_{RT}) ($S\ cm^{-1}$)	Activation energy (E_a) (meV)	Room temp. Seebeck coeff. (S_{RT}) ($\mu V\ K^{-1}$)	Ref.
NiCo ₂ O ₄	Spin coating	100	~65	–	16.67	–	–	[53]
NiCo ₂ O ₄	RF magnetron sputtering	100	~20	–	3.3×10^2	–	–	[52]
ZnRh ₂ O ₄	RF sputtering	100	–	2.1	0.7	37	+140	[55]
α -ZnRh ₂ O ₄	RF sputtering	100–300	–	2.1	1.9	29	+78	[104]
ZnRh ₂ O ₄	Pulsed laser deposition	100–300	55	2.74	2.75	22.1	+63.4	[54]
ZnCo ₂ O ₄	PLD	100–300	26	2.26	0.39	41.7	+131.4	[54]
ZnIr ₂ O ₄	PLD	100–300	60	2.97	3.39	46.9	+53.9	[54]

Table 12.3. Various deposition parameters of RF sputter-deposited spinel p-TCO films

Material	NiCo ₂ O ₄	ZnRh ₂ O ₄	a-ZnRh ₂ O ₄
RF power (W)	200	180	180
Base pressure (Pa)	1.33×10^{-4}	–	–
Sputtering gas(es)	O ₂ ^a	Ar + O ₂ (9:1 vol.%)	Ar + O ₂ (9:1 vol.%)
Sputtering pressure (Pa)	1.33	13.0	13.33
Target	Co–Ni alloys	ZnRh ₂ O ₄ pellet	ZnRh ₂ O ₄ pellet
Substrate	Quartz, sapphire, Si	Silica glass	Silica glass
Substrate temp. (°C)	Ambient	Ambient	Room temperature
Postannealing time (min)	–	60	–
Postannealing temp. (°C)	–	1,240	–
Reference	[52]	[55]	[105]

^a Sputtering was done in 100% oxygen atmosphere

configuration and the other with A-d⁹ (e.g., A = Pt, Pd) configuration. Generally, d¹⁰ cations show semiconducting behavior, whereas d⁹ cations show metallic conductivity [12–14]. As we are dealing with p-TCOs, therefore we will discuss only the d¹⁰-based delafossite materials here. The d¹⁰-based delafossite materials are two types: Cu- and Ag-based delafossite materials (CuBO₂ and AgBO₂; B: trivalent cation). Amongst various Cu-based delafossite materials, CuAlO₂ is the first and most important material in this group. Although this material is known to exist for nearly 50 years [106] and back in 1984, its p-type conductivity was first reported by Benko and Koffyberg [107], but Kawazoe et al. [100] first prepared it in transparent thin film form for possible application in p-TCO technology. The structural properties of this material were extensively studied by Ishiguro et al. [100–108, 108, 109, 109, 110]. The structure is shown in Fig. 12.2. It belongs to R $\bar{3}m$ (D_{3d}) space group with rhombohedral crystal structure [108]. Other p-TCO thin films belonging to this group are copper gallium oxide (CuGaO₂) and copper indium oxide (CuInO₂) [111–113]. The lattice parameters of these materials were reported in various papers [12–14, 107, 114, 115]. Also, the band structures of these materials were calculated by Yanagi et al. [116], Robertson et al. [117], and Ingram et al. [118] in detail.

Doped versions of some similar types of p-TCO thin films have also been reported which include iron-doped copper gallium oxide (CuGaO₂:Fe), calcium-doped copper indium oxide (CuInO₂:Ca), magnesium-doped copper scandium oxide (CuScO₂:Mg), magnesium-doped copper chromium oxide (CuCrO₂:Mg), calcium-doped copper yttrium oxide (CuYO₂:Ca), etc. [112, 113, 119–122]. Crystallographic data as well as band structure calculations of these materials had also been reported in various papers [114, 123, 124]. Preparation of some other highly resistive ($\sim 10^6 \Omega \text{ cm}$) new delafossite materials

such as $\text{CuFe}_{1-x}\text{V}_x\text{O}_2$ ($x = 0.5$), $\text{CuNi}_{1-x}\text{Sb}_x\text{O}_2$, $\text{CuZn}_{1-x}\text{Sb}_x\text{O}_2$, $\text{CuCo}_{1-x}\text{Sb}_x\text{O}_2$, $\text{CuMg}_{1-x}\text{Sb}_x\text{O}_2$, $\text{CuMn}_{1-x}\text{Sb}_x\text{O}_2$ ($x = 0.33$) in powder form had been reported by Nagrajan et al. [17, 125] (but no thin film preparation of these materials has been reported so far). Preparation of 10% Sn-doped $\text{CuNi}_{1-x}\text{Sb}_x\text{O}_2$ thin film has been reported by the same group [119, 125], having reasonable visible transparency (60%) and conductivity ($5 \times 10^{-2} \text{ S cm}^{-1}$). Electro-optical properties of various delafossite p-TCOs are furnished in Table 12.4.

It has been observed that most of the p-type semiconducting delafossite materials are Cu-based. Corresponding Ag-based delafossite materials are difficult to synthesize by simple solid-state reaction [119, 126]. The first report of Ag-based delafossite thin film was AgInO_2 , which is n-type in nature [127]. Later, Nagrajan et al. [128] reported that Mg-doped AgInO_2 powder ($\text{AgIn}_{1-x}\text{Mg}_x\text{O}_2$, $x = 0.1$), when treated with fluorine or high-pressure oxygen, p-type nature was observed with conductivity as low as $10^{-6} \text{ S cm}^{-1}$. A series of similar types of delafossite materials have been synthesized by the same group [128], but only in powder form, which include AgScO_2 , AgCrO_2 , AgGaO_2 , etc. All of these pellets showed very low conductivity ($\sim 10^{-6} \text{ S cm}^{-1}$) and no thin film preparations of these materials have been reported so far. On the other hand, the first report of Ag-based delafossite thin film with p-type conductivity was reported by Tate et al. [119], which is silver cobalt oxide (Ag_xCoO_2 , $x < 1$). The film showed reasonable conductivity ($2 \times 10^{-1} \text{ S cm}^{-1}$) and almost 50% transparency in the visible region with a direct bandgap value of 4.15 eV (shown in Figs. 12.8 and 12.9). The better conductivity of this film over other Ag-based delafossite materials may be attributed to the greater degree of mixing between Co 3d¹⁰ orbitals and O 2p⁶ orbitals, resulting in larger delocalization of holes [129, 130]. Doped versions of some other Ag-based delafossites have also been reported such as $\text{AgNi}_{1-x}\text{Sb}_x\text{O}_2$, $\text{AgZn}_{1-x}\text{Sb}_x\text{O}_2$ ($x = 0.33$), etc. [119] but only in powder form. Also, no comments on the nature of conductivity of these powders were given in the literature.

Regarding relative comparison between Cu-based delafossites and Ag-based delafossites, it has been suggested [131] that the former group can be better candidate for transparent conductor because of their greater hole mobility, which is due to the Cu 3d character of the valence band edge of Cu-based delafossites. Whereas for Ag-based delafossites, the valence band edge possesses O 2p character and d-manifold holes are more mobile than that of p-manifold [128].

12.3.5 Other Deposition Techniques: PLD, RF Sputter Deposition, Magnetron Sputtering with RTA, and Ion Exchange Method

Growth technique plays the most significant role on the properties of the films. Different deposition routes yield films with diverse structural,

Table 12.4. Delafossite p-TCO thin films with different doping concentrations and their respective optoelectrical parameters

Material	Dopant	Percentage of doping	Average film thickness (nm)	T (%)	E_g -direct (eV)	σ_{RT} ($S\ cm^{-1}$)	S_{RT} ($\mu V\ K^{-1}$)	Ref.
CuAlO ₂	Undoped	–	230	70	3.5	0.34	+214	[116]
CuGaO ₂	Undoped	–	500	80	3.6	0.063	+560	[111]
CuGa _{1-x} Fe _x O ₂	Fe	0.5	150	60	3.4	1.0	+500	[119]
CuIn _{1-x} Ca _x O ₂	Ca	0.07	170	70	~3.9	0.028	+480	[112]
CuCrO ₂	Undoped	–	250	40	~3.1	1.0	–	[121]
CuCr _{1-x} Mg _x O ₂	Mg	0.5	270	50	3.1	220.0	+150	[17, 121]
CuYO ₂	Undoped	–	200	60	~3.5	0.025	–	[17, 122]
CuY _{1-x} Ca _x O ₂	Ca	0.01–0.02	240	50	3.5	1.05	+275	[17, 122]
CuScO ₂ ^a	Undoped	–	110	40	~3.3	30.0	–	[17, 120]
CuSc _{1-x} Mg _x O ₂ ^b	Mg	0.05	220–250	80	3.3–3.6	~0.07	–	[119, 132]
				60	3.3–3.6	~0.1	–	
				25	3.3–3.6	~0.8	–	
				15	3.3–3.6	~20.0	–	
CuNi _{1-x} Sb _x Sn _y O ₂	Ni	0.66	~200	60	3.4	0.05	+250	[119]
	Sb	0.33						
	Sn	0.033						
AgCoO ₂ ^c	Undoped	–	150	50	4.15	0.2	+220	[119]

^a Maximum of 25% oxygen was intercalated

^b The variation of transparency of the films at the expense of conductivity was due to a variation of oxygen pressure from 3 (for most transparent film) to 15,000 Torr (for least transparent film). Also according to [132], the doping concentration of Mg was 1%

^c The Ag:Co ratio was 1.1:1

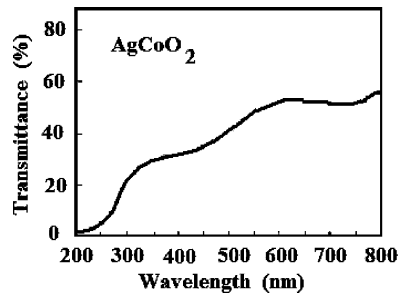


Fig. 12.8. Optical transmission of AgCoO_2 thin film (redrawn from [119] with permission)

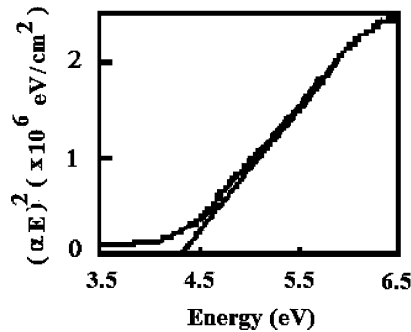


Fig. 12.9. Determination of direct bandgap of AgCoO_2 thin film (redrawn from [119] with permission)

optical, and electrical properties. Even for the same deposition technique, slight variation in the deposition parameters produces films with different properties. So it is very important to have a comparative study on the properties of various films produced by different deposition routes. Detailed description of different deposition techniques along with their schematic diagrams and related parameters is reported in various literatures [71, 74, 133–136]. Here we discuss briefly various deposition procedures used to deposit delafossite p-TCO thin films. PLD is a one of the important but relatively new and very efficient technique to deposit epitaxial films. Although a bit costly, but highly phase pure films with high-accuracy thickness can be prepared by this method. Delafossite p-TCO films prepared by this method include CuAlO_2 [100, 116, 137–139], CuGaO_2 [111, 137], $\text{CuInO}_2\text{:Ca}$ [112], CuScO_2 [140–142], etc. The deposition environment for most of the aforementioned reports was oxygen whereas the films were grown with an elevated substrate temperature. Postdeposition annealing was also done in most cases to induce excess oxygen for enhancing p-type conductivity as described later.

Sputtering is another popular thin film growth technique used extensively around the globe. As it is relatively cost-effective with respect to PLD and

large-area deposition is possible by this process, large-scale production of films for diverse applications can be done by this technique. Both reactive and nonreactive forms of direct current (DC), RF, magnetron, as well as ion beam sputtering techniques have been used for deposition of various delafossite p-TCOs. RF sputtering of CuAlO_2 [138, 139], $\text{CuGa}_{0.5}\text{Fe}_{0.5}\text{O}_2$ [119], $\text{CuCr}_{0.95}\text{Mg}_{0.05}\text{O}_2$ [121], CuScO_{2+y} , $\text{CuSc}_{0.95}\text{Mg}_{0.05}\text{O}_2$ [119, 120], $\text{CuNi}_{0.67}\text{Sb}_{0.3}\text{Sn}_{0.033}\text{O}_2$ [119, 125], AgCoO_2 [119], etc., has been reported. Pulsed magnetron sputtering of p- CuAlO_2 films was prepared by Alkoy and Kelly [126]. On the other hand, DC sputtering of CuAlO_2 thin film has been reported by us [15, 16, 57, 63, 143, 144], which is more cost-effective procedure. Also, in DC sputtering of oxide targets, the control of stoichiometry is almost automatic, whereas for RF sputtering, the target stoichiometry is to be adjusted suitably to compensate material loss from the substrate [74]. In all of the aforementioned reports, the targets used were the corresponding sintered pellets, arranged properly in the deposition chamber. Tables 12.5 and 12.6 represent various deposition parameters of delafossite p-TCO films synthesized by RF and DC sputtering. Also Figs. 12.10–12.15 show various characteristics of sputter-deposited delafossite p-TCO thin films. Reactive sputtering of delafossite p-TCOs has been used extensively by various researchers, which is discussed in details in later sections.

Table 12.5. Different deposition parameters of delafossite p-TCO films synthesized by RF magnetron sputtering

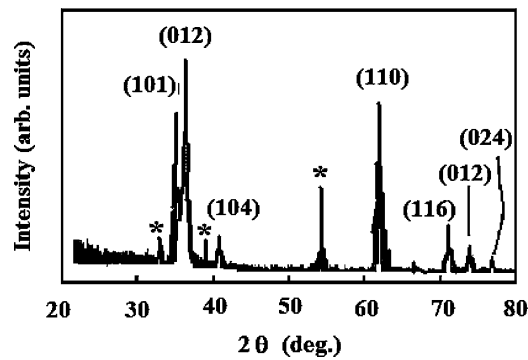
Material	CuAlO_2	$\text{CuGaO}_2\cdot\text{Fe}$	$\text{CuCrO}_2\cdot\text{Mg}$	$\text{CuNi}_{2/3}\text{Sb}_{1/3}\text{O}_2\cdot\text{Sn}$
RF power (W)	65	80	90	80
Electrode distance (mm)	40	30	38	–
Base pressure (Pa)	–	–	9.3×10^{-4}	–
Sputtering pressure (Pa)	4.53 (O_2 press)	13.33 (Ar: $\text{O}_2 = 4:1$)	1.33 (Ar press)	13.33 (Ar: $\text{O}_2 = 4:1/9:1$)
Target	CuAlO_2 pellet	$\text{CuGa}_{0.5}\text{Fe}_{0.5}\text{O}_2$ pellet	$\text{CuCr}_{1-x}\text{MgO}_2$ pellet	$\text{CuNi}_{0.67}\text{Sb}_{0.3}\text{Sn}_{0.03}\text{O}_2$ pellet
Substrate	$\alpha\text{-Al}_2\text{O}_3$ (001)	Fused silica	Fused quartz	SiO_2 , YSZ (100), Al_2O_3 (001)
Substrate temp. ($^\circ\text{C}$)	Ambient	100	450–750	500
Postannealing time (min)	90	90	2.5 (RTA in Ar)	180
Postannealing temp. ($^\circ\text{C}$)	1,050 ^a	800 (N_2 atmos.)	600–900	900 (in air) ^b
Reference	[138]	[119]	[121]	[119, 125]

^a Ex situ in a Lindberg box furnace containing small amount of CuAlO_2 powder

^b Also for some cases, RTA in air at 900°C was performed

Table 12.6. Deposition parameters of DC sputtering for CuAlO₂ thin film

Material	CuAlO ₂ thin film
Electrode distance (mm)	18
Target	Sintered CuAlO ₂ pellet
Substrate	Si (400) and glass
Sputtering voltage (V)	1,100
Current density (mA cm ⁻²)	10
Base pressure (Pa)	10 ⁻⁴
Sputtering pressure (Pa)	20
Sputtering atmosphere	Ar + 40 vol.% O ₂
Substrate temperature (°C)	180
Deposition time (min)	240
Postannealing time (min)	60
Postannealing temperature (°C)	200
Postannealing atmosphere (pressure)	O ₂ (20 Pa)
Reference	[143]

**Fig. 12.10.** XRD pattern of CuCr_{0.95}Mg_{0.05}O₂ thin film deposited by RF sputtering technique (redrawn from [121] with permission). *Asterisk marks* are from indium contacts

A combined process of magnetron sputtering and rapid thermal annealing (RTA) was used by Shy et al. [145] to prepare single crystalline delafossite p-type conducting CuAlO₂ thin films on sapphire substrate. Firstly, Cu₂O and Al₂O₃ precursor films on sapphire were deposited by reactive magnetron sputtering in an Ar + O₂ atmosphere. Cu and Al metal targets were used and reacted to form Cu₂O and Al₂O₃, respectively. The precursor films were deposited without substrate heating. Subsequent CuAlO₂ formation process was performed in air ambient by RTA. The specimens were heated up to 1,100 OC with a heating rate of 50 OC s⁻¹ and kept at the designated temperature for 40 min. A typical sandwich structure of Al₂O₃/Cu₂O/sapphire and the reaction mechanism before and after annealing is shown in Fig. 12.16.

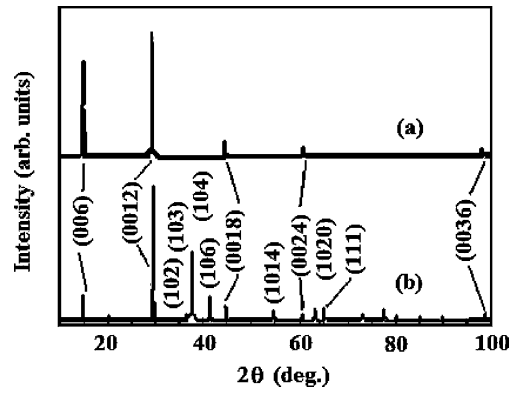


Fig. 12.11. XRD pattern of (a) AgCoO_2 thin film deposited by RF sputtering and (b) target (redrawn from [119] with permission)

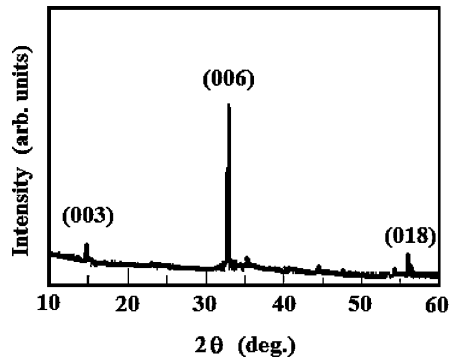


Fig. 12.12. XRD pattern of DC sputtered-deposited CuAlO_2 thin film (after [143])

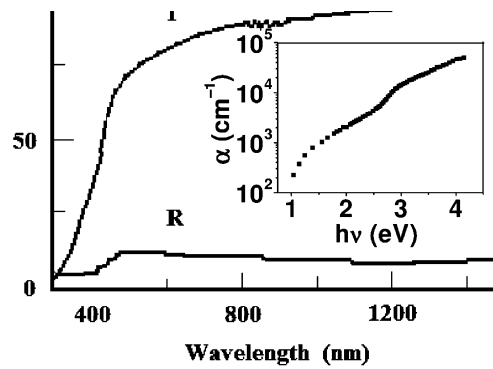


Fig. 12.13. Optical transmittance and reflectance spectra of CuAlO_2 thin film deposited by DC sputtering. *Inset* shows the spectral variation of absorption coefficients (α) (after [143])

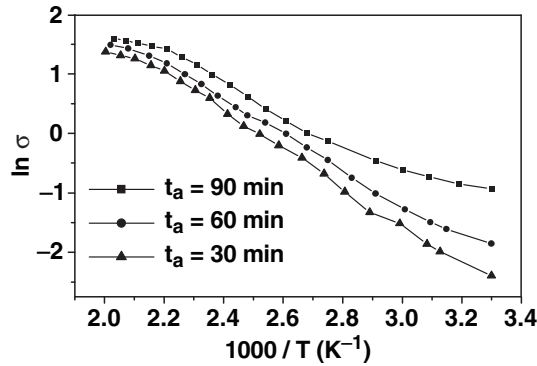


Fig. 12.14. Temperature variation of conductivity of $CuAlO_2$ thin film deposited by DC sputtering at different postdeposition oxygen annealing time (after [57])

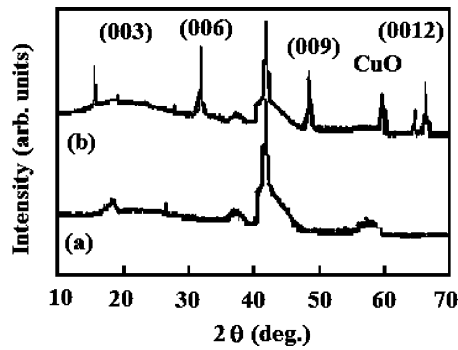


Fig. 12.15. XRD patterns of $CuAlO_2$ thin films deposited by RF magnetron sputtering: (a) as-deposited film and (b) postannealed at $1050^\circ C$ (after [138], reproduced by permission of ECS – The Electrochemical Society). The intensity axis is in logarithmic scale

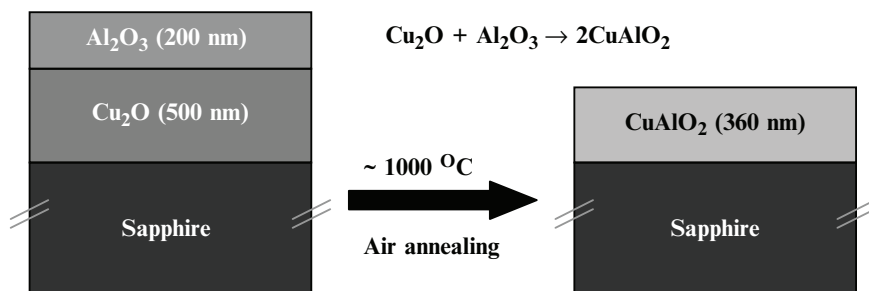


Fig. 12.16. Sandwich structure of $Al_2O_3/Cu_2O/sapphire$ before and after annealing. Also the typical reaction process is furnished

Ion exchange method is another interesting procedure by which several delafossite materials have been synthesized such as CuAlO_2 from LiAlO_2 [146], CuInO_2 from CuCl , Ag_xCoO_2 ($x < 1$) from NaCoO_2 and AgNO_3 [119], $\text{AgNi}_{0.67}\text{Sb}_{0.33}\text{O}_2$ from $\text{LiNi}_{0.67}\text{Sb}_{0.33}\text{O}_2$ and AgNO_3 , $\text{AgZn}_{0.67}\text{Sb}_{0.33}\text{O}_2$ from $\text{LiZn}_{0.67}\text{Sb}_{0.33}\text{O}_2$ and AgNO_3 [125], etc. Although no film preparation was reported by this method, this process may become an important target preparation procedure for PLD or sputtering.

Also, based on ab initio electronic structure calculations, new methods have been proposed by Yoshida and coauthors [147, 148] to fabricate high-conducting p- CuAlO_2 . They proposed that, in thermal nonequilibrium PLD or molecular beam epitaxy (MBE) crystal growth techniques, induction of high concentration of Cu vacancies in the material, to form impurity band, by reducing the Cu vapor pressure during deposition might enhance the p-type conductivity in the material. On the other hand, doping of Mg or Be at Al sites to form acceptor levels by decreasing the Al vapor pressure and increasing the Cu vapor pressure during low-temperature PLD, MBE, or MOCVD process might also increase the p-type conductivity of the material (Tables 12.7 and 12.8).

12.3.6 Reactive Sputtered p-TCO

It is well known that reactive sputtering has the advantage over conventional (RF or DC) sputtering from oxide targets, due to the fact that plasma density would be better in former case due to the high conductivity of elemental targets or metal powders, leading to better uniformity of the films. Also, the intermediate step of sintering procedure to form the target pellet can be avoided by this method. Both RF magnetron reactive cosputtering and DC reactive sputtering have been adopted by various groups. As DC sputtering can be applied conveniently for low resistive targets, whereas RF sputtering is convenient only for high resistive (or insulating) targets, therefore, keeping an eye on the cost-effectiveness of the deposition techniques, various groups concentrated their attention more onto the DC reactive sputtering technique to deposit p-TCO films from metal targets.

As far as reactive sputtering of spinel p-TCO films is concerned, Kim and coauthors [37] deposited ZnCo_2O_4 thin films on SiO_2 (200 nm)/Si substrate by reactive magnetron sputtering technique. This group had used a combinatorial approach of DC and RF magnetron cosputtering of elemental Co and Zn targets in an oxygen-diluted Ar atmosphere and at an elevated substrate temperature (600°C). For Co targets, they have used DC source with a sputtering power of 200 W, whereas, RF source had been used for Zn target with an RF forward power of 100 W and a fixed total sputtering power ratio ($P_{\text{Co}}/P_{\text{Zn}}$) of 2.0. They have observed that the sputtering power ratio between Co and Zn targets is a critical growth parameter for the formation of the spinel phase. Details of various reactive sputtering parameters for reactive deposition of spinel ZnCo_2O_4 have been furnished in Table 12.9.

Table 12.7. Optical and electrical properties of delafossite p-CuAlO₂ thin films synthesized by various growth techniques

Growth technique	Thickness (nm)	Average visible transmittance (%)	Room temp. conductivity (S cm ⁻¹)	E_a (meV)	Carrier concentration (cm ⁻³)	Room temp. Seebeck coeff. ($\mu\text{V K}^{-1}$)	Ref.	Remarks
PLD	500	70	0.095	~200	1.3×10^{17}	+183	[100]	–
PLD	230	80	0.34	220	2.7×10^{19}	+214	[116]	Films were postannealed in O ₂ atmosphere (1.3 Pa)
RF magnetron sputtering	180	85	–	–	–	–	[138]	Preliminary Hall and TEP measurements confirmed p-type conductivity
Pulsed magnetron sputtering	40–240	85	0.1–0.2	–	–	–	[126]	The indirect bandgap was estimated to be 1.6 eV
DC sputtering	500–700	80	0.08	260	3.7×10^{17}	+128	[143]	Films were postannealed in O ₂ atmosphere (20 Pa) for 60 min
DC sputtering	500	85	0.39	196	1.2×10^{18}	+213	[57]	Films were postannealed in O ₂ atmosphere (20 Pa) for 90 min
MOCVD	250	40	2.0	120	2.6×10^{19}	–	[149]	The films were a mixture of CuAlO ₂ , Cu ₂ O, and CuAl ₂ O ₄

(continued)

Table 12.7. (continued)

PE-MOCVD	120	40	17.08	32	1.17×10^{20}	–	[150, 151]	For those samples annealed in air for 5 min (at 350°C)
E-beam evaporation	–	50–85	1.0	–	10^{18} – 10^{20}	–	[152]	Hole concentration decreases with increasing water vapor pressure
RTA	360	60	0.57	–	–	–	[145]	RTA was performed over 1,000°C
Dip coating	3,500	90	–	–	–	–	[153]	Films were annealed in air (at 500°C) for 180 min
Dip coating	1,000	–	5×10^{-3}	–	–	–	[154]	Results given for films deposited via nitrate route
Spin-coating technique	420	60	2.4	140	5.4×10^{18}	–	[155]	Film is nanocrystalline in nature with grain size around 14–16 nm
Spray pyrolyses	1,000	30–70	–	–	–	–	[156]	Transmittance increases as Cu:Al ratio approaches to 1.0
Sol-gel synthesis	1,100	–	0.004	–	–	–	[157]	High resistivity is due to porous structure of the film

Table 12.8. Optical and electrical properties of different Cu- and Ag-based delafossite p-TCO thin films (other than CuAlO₂) synthesized by RF sputtering technique

Material	Method	Thickness (nm)	Average visible transmittance (%)	Room temp. conductivity (S cm ⁻¹)	E_a (meV)	Carrier concentration (cm ⁻³)	Room temp. Seebeck coeff. (μ VK ⁻¹)	Ref.	Remarks
CuGaO ₂ :Fe	RF sputtering	150	50–70	1.0	100	–	+500	[119]	Films were postannealed in N ₂ atmosphere at 800°C for 90 min and 50% Ga replaced by Fe
CuScO ₂	RF sputtering	110	40	30.0	110	–	–	[120]	Actual formula was given as CuScO _{2+y}
CuScO ₂ :Mg	RF sputtering	250	15	20.0	95	–	–	[119]	5% Mg doping for Sc. Also the variation in σ_{RT} and T was due to change in postdeposition O ₂ annealing pressure
CuCrO ₂	RF sputtering	200–300	70 30	0.08 1.0	– –	– –	– –	[119] [119, 121]	–
CuCrO ₂ :Mg	RF sputtering	200–300	30–40	220	20 ^a	–	+150	[119, 121]	5% Cr replaced by Mg
CuNi _{0.67} Sb _{0.3} O ₂ :Sn	RF sputtering	150–200	60	0.05	170	–	+250	[119, 125]	10% Sb replaced by Sn
AgCoO ₂	RF sputtering	150	40–60	0.20	70	–	+220	[119]	Ag:Co = 1.1:1.0

^a For low value of E_a , the word “activation” should be used with caution

Table 12.9. RF magnetron reactive cosputtering of spinel and delafossite p-TCO films

Material	ZnCo ₂ O ₄	Cu–Al–O films (a mixture of CuAlO ₂ and CuO)
RF power (W)	Zn power: 100 Co power: 200 ^a	Al power: 60–110 ^b Cu power: 30
Targets	Metallic Zn and Co	Metallic Cu and Al
Substrate	SiO ₂ (200 nm)/Si	Glass
Substrate temp. (°C)	600	100
Base pressure (Pa)	2.0×10^{-4}	–
Deposition pressure (Pa)	1.33	–
Sputtering atmosphere	Ar + O ₂ ^c	Ar + 5% O ₂
Postannealing	–	None
Reference	[37]	[158]

^a For Co target, DC source had been used

^b For Al power, 110 W single phase amorphous CuAlO₂ was formed

^c O₂ partial pressure is varied from 10 to 90%

This group had also varied the ratio of oxygen partial pressure to a constant total working pressure (10 mTorr) during deposition from 10 (with O₂ partial pressure 1 mTorr) to 90% (with O₂ partial pressure 9 mTorr) and observed that the films deposited with a oxygen partial pressure ratio less than 70% showed n-type conductivity, whereas, those deposited above 80% oxygen partial pressure ratio are p-type conducting [37]. Figure 12.17 shows various electrical parameters of ZnCo₂O₄ thin film under different oxygen partial pressure ratio. Also, Table 12.11 describes various optoelectrical parameters of spinel p-ZnCo₂O₄ thin films prepared by reactive magnetron cosputtering technique.

Reactive sputtering of delafossite p-TCO thin films involves both RF and DC reactive sputtering techniques. For RF sputtering, Ong and Gong [158] used RF magnetron reactive cosputtering of Cu and Al metal targets to synthesize transparent p-type Cu–Al–O films (a mixture of delafossite CuAlO₂ and CuO). This group used 30 W fixed RF power for Cu target, but a variable power (60–110 W) for Al target, as the sputtering yield of Al is less than that of Cu in Ar + O₂ environment. Various sputtering conditions for the film growth are furnished Table 12.9. With varying Al power, they obtained Cu–Al–O films with a varied Cu/Al ratio from 10 to 0.9%, and at an Al power of 110 W, they obtained single phase amorphous p-CuAlO₂ thin film. Also from the absorption data, they have observed a blueshift of the bandgap of this multiphase film (mixture of CuAlO₂ and CuO) with an increase in the Al content within the film. Whether this bandgap widening is due to Burstein-Moss shift [159] or may be attributed to the quantum confinement effect put forward by Brus [160] is still not clear and intense research is needed in this direction to explore the exact mechanism. Figures 12.18 and 12.19 show the

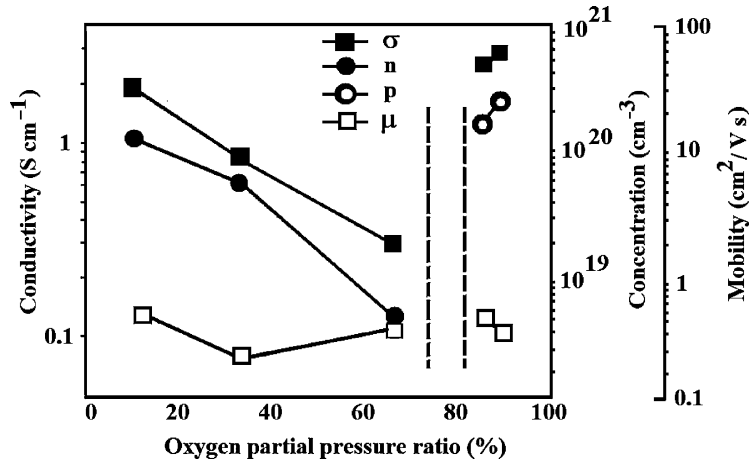


Fig. 12.17. Conductivity (σ), electron concentration (n), hole concentration (p), and mobility (μ) of $ZnCo_2O_4$ thin film at various oxygen partial pressure ratio (after [37])

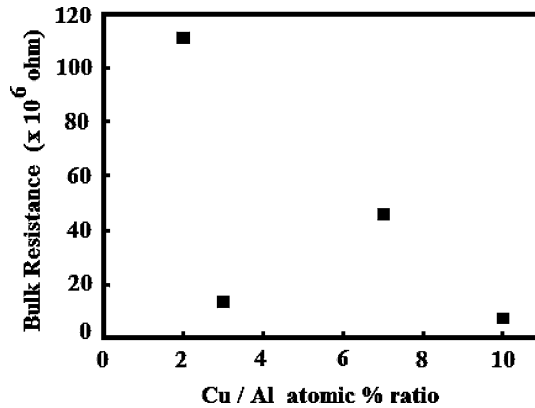


Fig. 12.18. Bulk resistance of RF magnetron reactive sputter-deposited Cu–Al–O thin films with different Cu/Al atomic ratio and at different Al power (from 60 to 90 W) (after [158])

variation in the bulk resistance and optical bandgap values of Cu–Al–O thin films with different Cu/Al atomic ratio, respectively.

As far as DC reactive sputtering is concerned, Tsuboi et al. [161, 162] used facing targets of Cu and Al metals and a rotating substrate to synthesize $CuAlO_2$ films by DC reactive sputtering. A schematic diagram of the apparatus is shown in Fig. 12.20. As shown in the figure, the discharge plasma could be confined between the facing targets by magnetic field and the substrate was placed outside the plasma region to avoid bombardments of high-energy particles. The sputtered Cu and Al atoms were alternately

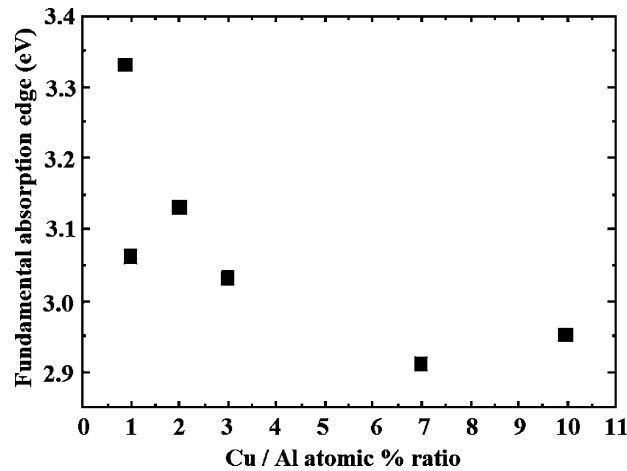


Fig. 12.19. Blueshift of fundamental absorption edge of RF magnetron reactive sputter-deposited Cu–Al–O films with different Cu/Al atomic ratio (after [158])

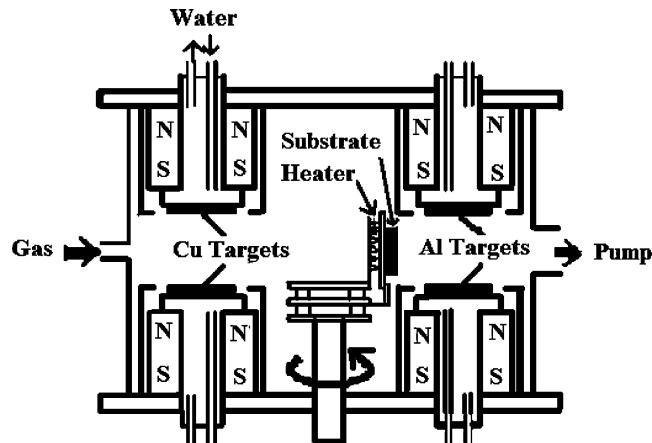


Fig. 12.20. DC reactive sputtering system with two pairs of opposite facing targets and a rotating substrate (after [161])

deposited on the quartz substrate at 300°C for about 4 h by controlling a pulse motor connected with the substrate holder. The sequential period of Cu deposition (t_{Cu}) was fixed to 1 s, whereas the same for Al (t_{Al}) was varied from 3 to 15 s to vary the Cu/Al ratio in the film.

The total film thickness was in the range of 400–800 nm. The films were postannealed at temperatures of 500–1050°C for 4 h in the nitrogen flow under atmospheric pressure. Various sputtering parameters for this film growth are furnished in Table 12.10. Figure 12.21 shows the composition of the film with different postannealing time. The [Cu]/[Al] ratio in the as-deposited films decreased with increasing t_{Al} . Figure 12.22 shows the optical transmis-

Table 12.10. Various sputtering parameters of reactive DC sputtered delafossite p-TCO thin films

Material	CuAlO ₂ thin film	CuAlO ₂ thin film	CuAlO ₂ thin film ^a
Target	Elemental Cu and Al metal (facing) targets	Mixture of Cu + Al metal powder pellets	Cu/Al alloy (with 1:3 ratio)
Electrode distance (mm)	–	18	65
Sputtering voltage (V)	Cu-facing targets = 750 Al-facing targets = 350	1,000	292–394
Current density (mA cm ⁻²)	Cu-facing targets ~1.17 Al-facing targets ~7.0	12	200–300 mA (current)
Base pressure (Pa)	–	10 ⁻⁴	5 × 10 ⁻⁴
Sputtering pressure (Pa)	0.53	20.0	4.0
Sputtering atmosphere	Ar + O ₂ (4:1)	Ar + O ₂ (3:2)	Ar + O ₂
Substrate	Quartz (rotating)	Si (400) and glass	Glass
Substrate temperature (°C)	300	200	250
Deposition time (min)	240	240	–
Postannealing time (min)	240	60	–
Postannealing temp. (°C)	> 700	220	–
Postannealing atmosphere	N ₂ (ambient pressure)	O ₂ (20 Pa)	–
Reference	[161]	[163, 164]	[165]

^a This process involved DC reactive magnetron sputtering

sion spectra of DC reactive sputter-deposited p-CuAlO₂ thin film at different Cu/Al ratios.

Similarly, DC reactive magnetron sputtering of p-CuAlO₂ film was done by Reddy and coauthors [165], where a target of Cu/Al alloy (with 1:3 ratio) was used to deposit CuAlO₂ film on glass substrate. This group has systematically studied the change in electrical, optical, and structural properties of p-CuAlO₂ thin films with a variation in the oxygen partial pressure during deposition. Figures 12.23 and 12.24 show the variation in different electrical and optical properties of these films with respect to oxygen partial pressure. It must be mentioned here that, in most of the sputtering procedures indicated

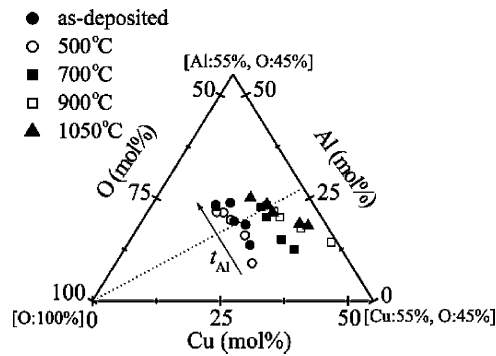


Fig. 12.21. Composition of as-deposited and postannealed p-CuAlO₂ thin films (after [161])

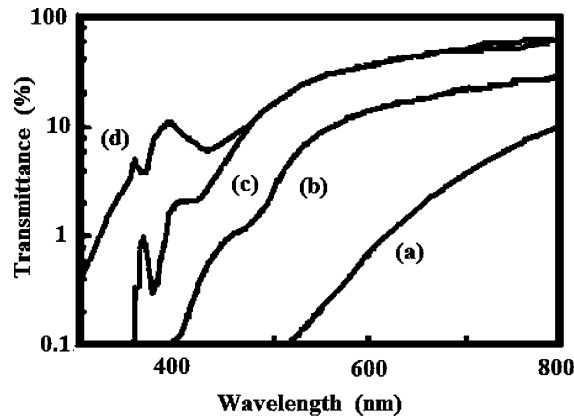


Fig. 12.22. Optical transmission spectra of p-CuAlO₂ thin films postannealed at 1050°C. Cu/Al ratio in the films varied from (a) 1.8, (b) 1.7, (c) 1.1, and (d) 0.7 (after [161])

above, the sputtering atmosphere was taken as Ar and O₂ and the depositions were done in an elevated substrate temperature. Postannealing of the films was also performed in many cases to get better p-type conductivity. In some cases, RTA of the films was also done to get higher crystallinity and transparency [120, 121]. Various deposition parameters of DC reactive sputter-deposited delafossite p-TCO thin films are furnished in Table 12.10. Also various electro-optical parameters of different DC reactive sputtered thin films are furnished in Table 12.11.

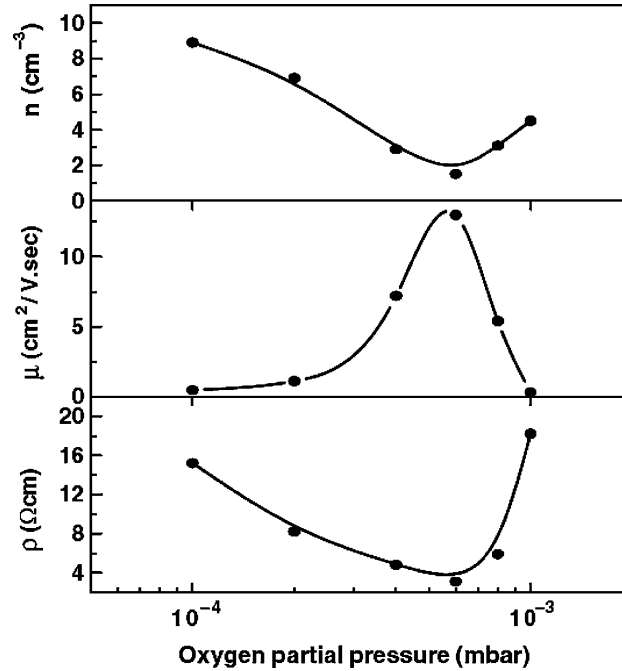


Fig. 12.23. Variations in electrical resistivity (ρ), Hall mobility (μ), and carrier concentration (n) of DC reactive sputtered p-CuAlO₂ thin films (after [165])

12.4 Transparent Junctions Based on Spinel and Delafossite Oxides

Junctional devices fabricated by both n- and p-types of TCO thin films are the key structure for “Invisible Electronics” [56]. The simplest of them is the p–n junction diodes with rectifying properties. The importance of these types of devices lies in the fact that “functional windows” can be fabricated by these devices, which would transmit the visible solar radiation but absorb the UV part of it [100]. Thus simultaneously, these devices can act as “UV shields” as well as “electricity generators” by the UV absorption. Fabrication of a number of all-TCO diodes based on spinel and delafossite p-TCO films has been reported, which includes both p–n and p–i–n homojunctions and heterojunctions as well as transparent field-effect transistors (TFETs). A schematic diagram of all-TCO diode is shown in Fig. 12.25.

As far as all-TCO junction based on spinel structure is concerned, Ohta et al. [166] first reported p–n heterojunction of the form p-ZnRh₂O₄/ n-ZnO on indium tin oxide (ITO)-coated YSZ (111) substrate. The n- and p-layers were deposited by PLD technique. A schematic diagram of the structure is shown in Fig. 12.26 and corresponding I–V curve is given in the inset. The curve shows rectifying properties with threshold voltage around 2.0 V.

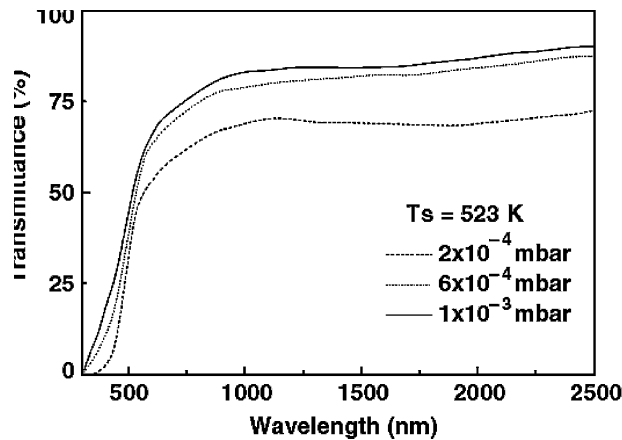


Fig. 12.24. Optical transmittance spectra of DC reactive magnetron sputtered p-CuAlO₂ film at different oxygen partial pressures (after [165])

Most of the groups have chosen ZnO as the n-layer mainly because of less lattice mismatch between p-layers, which is necessary to fabricate proper rectifying junctions. For n-ZnO/p-ZnRh₂O₄ rectifying junction, Ohta et al. [166] have selected ZnO epitaxial layer as the n-type material mainly because of the sixfold symmetrical oxygen configuration in (0001) plane of ZnO, which is similar to that in the (111) plane of ZnRh₂O₄ with the sixfold symmetry. The mismatch is very low and more importantly, no chemical reaction was expected to take place between the two layers even at high temperature because no other crystalline phases have been reported in the equilibrium Zn–Rh–O system [166]. The same group has also demonstrated amorphous oxide p–n junction diodes based on other crystalline material spinel ZnRh₂O₄ [104,167]. The diode was formed on glass and plastic substrates with ITO and Au as ohmic contacts. The structure of the diode is shown in Fig. 12.27 and the corresponding I–V characteristic is shown in the inset. Some of the diode characteristics are furnished in Table 12.12.

Amorphous semiconductors are highly favorable for large-scale production of many devices like solar cells, flat panel displays, etc. The advantage of using amorphous materials in these devices lies in the fact that low-temperature deposition of amorphous thin films on large substrates is possible and also the problem of lattice mismatching in p–n junctions can be minimized by using amorphous materials [167]. Therefore, tremendous opportunities lie ahead in the field of amorphous oxide-based p–n junctional devices.

As far as delafossite p-TCO-based transparent junctions are concerned, Hoffman et al. [168] fabricated p–i–n heterojunction of the form p-CuYO₂:Ca/i-ZnO/n-ITO. The I–V characteristics are shown in Fig. 12.28. They have observed visible transparency of the structure around 35–65%. Similarly, Jayaraj et al. [122,169] fabricated p–n heterojunction using p-CuY_{1-x}Ca_xO₂

Table 12.11. Optical and electrical properties of different spinel and delafossite p-TCO thin films synthesized by reactive sputtering techniques

Material	Growth technique	Thickness (nm)	Average visible transmittance (%)	Room temp. conductivity (S cm^{-1})	E_a (meV)	Carrier concentration (cm^{-3})	Room temp. Seebeck coeff. ($\mu\text{V K}^{-1}$)	Ref.	Remarks
ZnCo_2O_4	RF magnetron reactive cosputtering	400	–	1.5–2.0	–	2.41×10^{20}	–	[37]	Oxygen partial pressure ratio more than 80% gives spinel p- ZnCo_2O_4 films
CuAlO_2	RF magnetron reactive cosputtering	250	20–80	–	–	–	–	[158]	Small amount of CuO was present in the film
CuAlO_2	Reactive DC sputtering	400–800	50–60	0.01–0.1	–	–	–	[161]	With facing metal targets and rotating substrate. Films were annealed at $1,050^\circ\text{C}$ in N_2 atmosphere
CuAlO_2	Reactive DC sputtering	500	85	0.22	250	4.4×10^{17}	+115	[154, 163]	Target was Cu + Al metal powder pellets
CuAlO_2	Reactive DC magnetron sputtering	120–130	70–75	0.32	–	4.5×10^{17}	–	[165]	The best electrical properties were obtained at 6×10^{-4} mbar

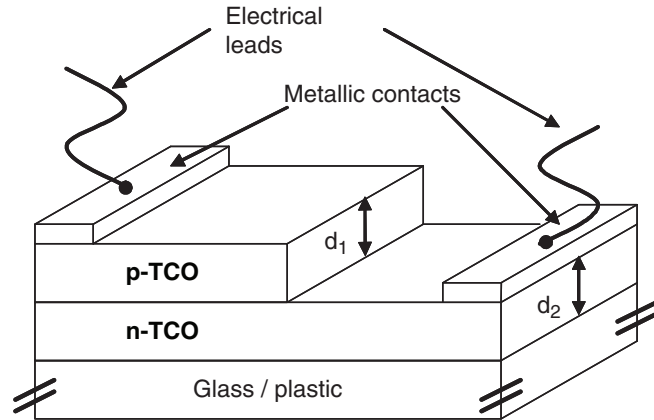


Fig. 12.25. All-TCO p-n junction diode on glass or plastic substrate

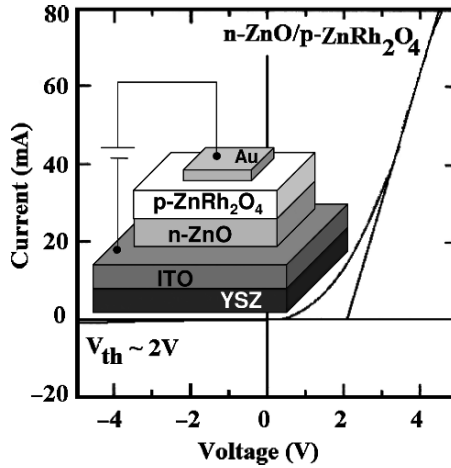


Fig. 12.26. Current–voltage characteristics of ITO/n-ZnO/p-ZnRh₂O₄/Au diode (after [166]). *Inset* is the schematic structure of the diode

($x = 0.01-0.02$)/n-Zn_{1-x}Al_xO ($x = 0.02$) structure. They observed rectifying I–V characteristics with a turn-on voltage between 0.4 and 0.8 V (shown in Fig. 12.29).

Also, Tonooka et al. [170] reported the fabrication of n-ZnO/p-CuAlO₂ diode structure with rectifying characteristics and observed a photovoltaic effect (as large as 80 mV) under illumination of blue radiation. Although the performance of the diode was restricted by the low crystallinity of the CuAlO₂ layer, the forward-to-reverse current ratio showed a moderate value of 90 between -1.5 and $+1.5$ V. Also the transparency of the structure was 40–70% in the visible region. The diode structure and transparency of the diode are shown in Fig. 12.30. We have recently reported the fabrication of

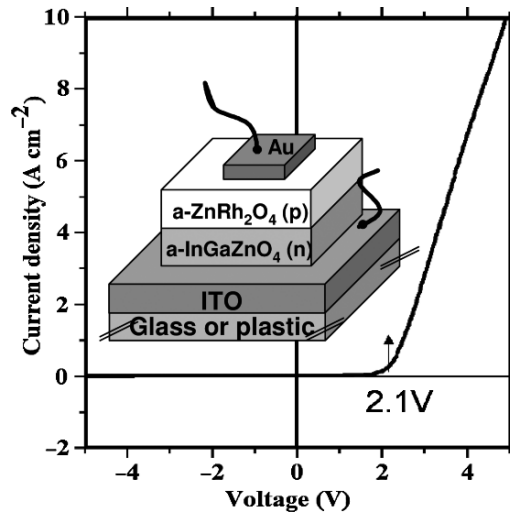


Fig. 12.27. Current–voltage characteristics of amorphous oxide-based diode of the form glass/ITO/n-InGaZnO₄/p-ZnRh₂O₄/Au (after [104]). *Inset:* corresponding device structure

p-CuAlO_{2+x}/n-Zn_{1-x}Al_xO heterojunction diode by a combination of cost-effective physical (sputtering) and wet-chemical (sol-gel) processes [146]. The diode shows 60% visible transparency with turn-on voltage around 0.8 V. The approximate equilibrium energy band diagram depicted that this low turn-on voltage is due to the presence of some midgap energy levels, which might have been induced as a result of excess oxygen intercalation during sputtering of the p-layer.

Also, some unintentional impurity incorporation during sol-gel process may not be ruled out as another reason for the formation of these midgap energy levels [146]. The I–V characteristics and optical transparency of the diode are shown in Fig. 12.31. Also, some of the electro-optical properties of all the aforementioned junctions are furnished in Table 12.12.

Besides heterojunctions, fabrication of p–n homojunctions was also reported by few authors. Importance of the homojunctions lies in the fact that lattice matching is supposed to be automatic during the formation of diodes. First all-delafossite p–n homojunction diode was fabricated by Yanagi et al. [113]. The diode structure was of the form of YSZ (111)/ITO/p-CuInO₂:Ca/n-CuInO₂:Sn/ITO (shown in Fig. 12.32). Calcium- and tin-doped copper indium oxide films were used as the p- and n-layers, whereas ITO was used as metallic electrodes. They observed rectifying properties of the junction with turn-on voltage ~ 1.8 V, which is shown in Fig. 12.32. Various electro-optical parameters of different all-transparent homojunction diode are furnished in Table 12.12.

Table 12.12. Parameters of deferent all-transparent diodes

Diode structure	n-ZnO/ p- ZnRh ₂ O ₄	a-InGaZnO ₄ (n)/a- ZnRh ₂ O ₄ (p)	n ⁺ -ITO/ i-ZnO/p ⁺ - CuYO ₂ :Ca	n-Zn _{1-x} Al _x O/ p-CuY _{1-x} Ca _x O ₂	n-ZnO/ p-CuAlO ₂	n-CuInO ₂ :Sn/ p-CuInO ₂ :Ca	n-Zn _{1-x} Al _x O/ p-CuAlO _{2+x}	
Thickness (nm)	p-Layer	–	300	300	300	400	400	500
	i-Layer	–	–	250	–	–	–	–
	n-Layer	–	300	200	250	400	400	600
Carrier concen- tration (cm ⁻³)	p-Layer	–	–	1 × 10 ¹⁹	~10 ¹⁹	–	–	2.6 × 10 ¹⁷
	i-Layer	–	–	5 × 10 ¹⁹	–	–	–	–
	n-Layer	–	4.2 × 10 ¹⁶	~10 ²⁰	9.6 × 10 ²⁰	–	–	3.0 × 10 ¹⁷
Substrate	ITO-coated YSZ (111)	Glass/plastic	Glass	Glass	Glass	YSZ (111)	Glass	Glass
Deposition technique	p-Layer	PLD	RF sputtering	Reactive coevaporation	Reactive coevaporation in O ₂ atmosphere	PLD	PLD	Sputtering
	i-Layer	–	–	RF magnetron sputtering	–	–	–	–
	n-Layer	PLD	RF sputtering	RF sputtering	RF magnetron sputtering	PLD	PLD	Sol-gel dip coating
Electrodes	p-Side	Au	Au	In	In	ITO	ITO	Ag
	n-Side	ITO	ITO	In	ITO	n ⁺ -ZnO	ITO	Ag
Turn-on voltage (V)	~2.0	~2.1	~4.0	0.4-0.8	0.4-1.0	1.8	0.8	0.8
Forward-to-reverse current ratio	–	10 ³ at ±5.0 V	60 at ±4.0 V	190 at ±3 V	90 at ±1.5 V	10 at ±4.0 V	30 at ±4.0 V	
Reference	[166]	[104, 167]	[168]	[122, 168, 169]	[170]	[113]	[146]	
Remarks	The diode exhibits photovoltage with UV-light illumination	The n- and p-layers were deposited at room temperature	The ZnO layer becomes semi-insulating after RTA at 600°C with n ~ 10 ¹⁷ cm ⁻³	The diode showed 40% transparency in the visible region	ZnO layer grown at 250°C showed good rectifying property	The diode showed 60-80% transparency in the visible region	No postannealing was done for the p-layer during diode formation	

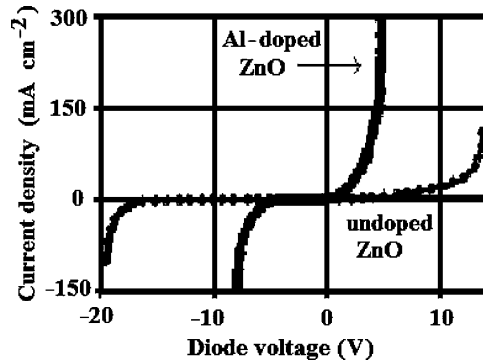


Fig. 12.28. I-V characteristics of n^+ -ITO/ i -ZnO/ p^+ -CuYO₂:Ca heterojunction diode for undoped and Al-doped intrinsic ZnO layer (after [168])

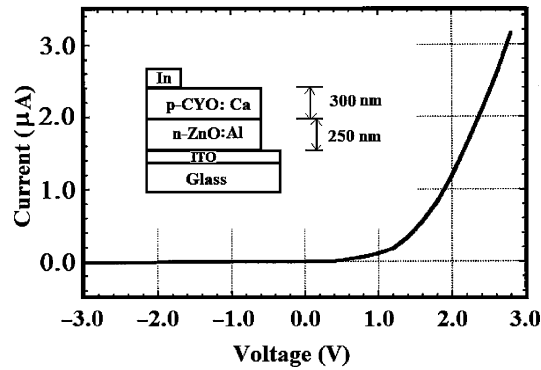


Fig. 12.29. I-V curve of p -CuYO₂:Ca/ n -ZnO:Al transparent diode (after [122]). Inset shows the corresponding diode structure

Another important area in the field of “Transparent Electronics” is the fabrication of TFETs [89]. Prins et al. [171,172] reported the fabrication of ferroelectric TFETs, based on transparent SnO₂:Sb thin films. They have observed the field-effect mobility around $10 \text{ cm}^2 \text{ V}^{-1} \text{ s}^{-1}$, with an on/off current ratio $\sim 10^4$. Later various groups [173–175] reported the fabrication of ZnO-based TFETs with reasonable device properties. Recently, Nomura, Ohta, and coauthors [176,177] reported the successful fabrication of high mobility top-gate TFETs based on single crystalline transparent InGaO₃(ZnO)₅ thin film. The device shows the mobility as high as $80 \text{ cm}^2 \text{ V}^{-1} \text{ s}^{-1}$ with on/off current ratio $\sim 10^6$ and more than 80% transparency in the visible and near-infrared region. A schematic diagram of TFET structure is shown in Fig. 12.33. The deposition techniques for the fabrication of these TFETs include PLD [171,172,174], ion beam sputtering [173], RF magnetron sputtering [175], reactive solid-phase epitaxy [176], etc. But, till date (as far as literature survey depicts),

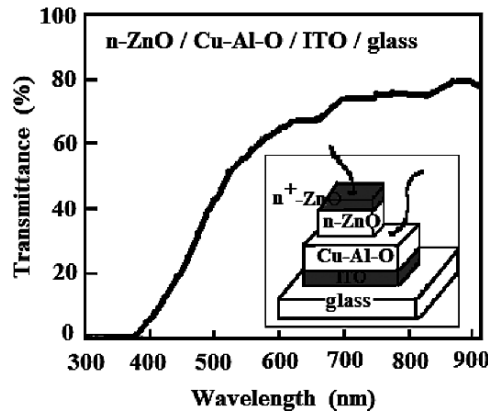


Fig. 12.30. Optical transparency of n-ZnO/p-Cu–Al–O diode. *Inset* shows the corresponding diode structure (after [170])

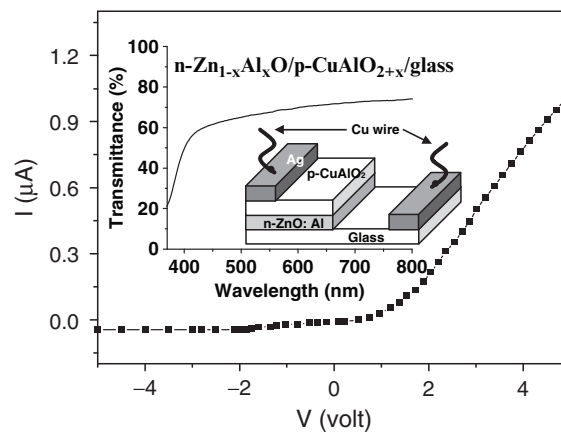


Fig. 12.31. Rectifying I–V curve of p-CuAlO_{2+x}/n-Zn_{1-x}Al_xO diode. *Inset*: optical transmission of the diode structure (after [146])

there are no reports of TFETs based on any spinel or delafossite p-TCOs. In spite of that, these reports provide a significant step toward the realization of “Invisible Electronics.”

12.5 Origin of p-Type Conductivity in Wide-Bandgap Spinel and Delafossite Oxide Materials

It has been found that most of the existing TCOs are n-type, whereas it is very difficult to prepare binary metal oxides with p-type conductivity. A possible reason for this has been described by Kawazoe et al. [100,137], where

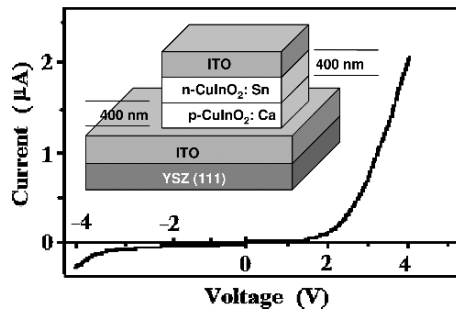


Fig. 12.32. I-V characteristics of all-delafossite diode consist of p-CuInO₂:Ca/n-CuInO₂:Sn layers as shown in Fig. IX-6(a) (after [113])

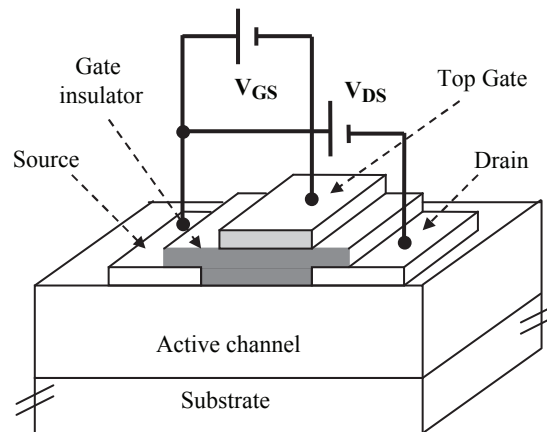


Fig. 12.33 Schematic diagram of top-gated TFET structure (after [176])

they argued that this is probably because of the electronic structure of these metal oxides. Strong localization of holes (it can be successfully introduced by intentional substitutional doping or by producing nonstoichiometry within the material) at oxygen 2p levels or an upper edge of the valence band due to high electronegative nature of oxygen, i.e., this localization is due to the ionicity of metallic oxides. O 2p levels are far lower lying than the valence orbit of metallic atoms [178], leading to the formation of deep acceptor level by the holes. In other words, the holes, therefore, have high probability to be localized around the oxygen atoms. Hence these holes require high enough energy to overcome large barrier height to migrate within the crystal lattice, resulting in poor conductivity and hole mobility.

A possible solution proposed by Kawazoe et al. [137] is to introduce a “degree of covalency” in the metal-oxygen bondings to induce the formation of an extended valence band structure, i.e., the valence band edge should be modified by mixing orbitals of appropriate counter cations that have energy-filled levels comparable to O 2p level. This would reduce the strong coulombic

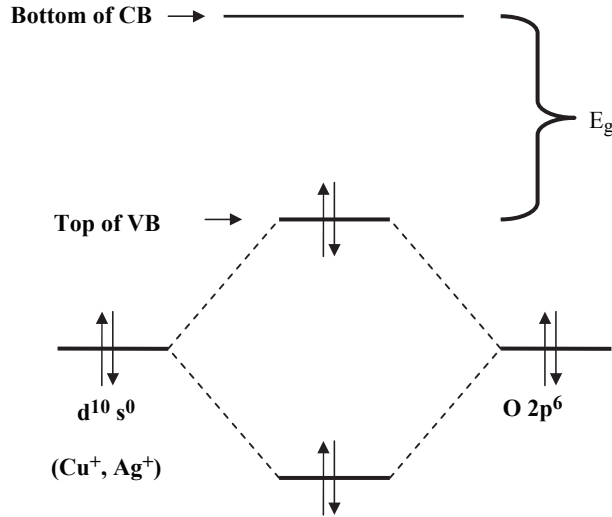


Fig. 12.34. CMVB method. Energy levels are not to the scale (after [137])

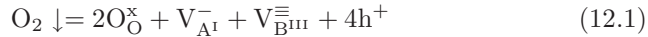
force by oxygen ions and thereby delocalizing the holes. This is the essential approach to obtain p-TCO, which is called “chemical modulation of the valence band (CMVB)” [137].

But the next requirement is the choice of appropriate cationic species that will serve for CMVB technique. Investigations showed that the required cationic species are $3d^{10}$ -closed shell of Cu^+ ions and $4d^{10}$ -closed shell of Ag^+ ions [137, 178]. Although some transition metal cations with open d-shell may fulfill the energy requirement [179] for CMVB technique, but they usually show strong coloration due to d-d transition, which is expected but not wanted for transparent materials. Hence, focus had been concentrated on the cations mentioned above, with closed ($d^{10} s^0$) electronic configuration. Figure 12.34 shows a schematic illustration of CMVB technique. Both of the atomic orbitals are occupied by electron pairs, and the resulting antibonding level becomes the highest occupied level, i.e., the valence band edge.

Next is the structural requirement for designing p-TCO materials. Tetrahedral coordination of oxygen ions is advantageous for p-type conductivity, as it acts in reducing the localization behavior of 2p electrons on oxide ions [137]. The valence state of the oxide ions can be expressed as sp^3 in this conformation. Eight electrons (including $2s^2$) on an oxide ion are distributed in the four σ bonds with the coordination cations. This electronic configuration reduces the nonbonding nature of the oxide ions and increases the delocalization of holes at the valence band edge (that is why Cu_2O is a p-type conducting oxide [180–183]). But Cu_2O , although p-type in nature, has rather small bandgap (2.17 eV) [181]. This is probably because of the three-dimensional interactions between $3d^{10}$ electrons of neighboring

Cu⁺ ions. It is expected that the low-dimensional crystal structure would suppress this interaction [116]. As we are interested in TCOs, bandgap of the material (E_g) should be greater than 3.1 eV. Hence enlargement of bandgap would be another structural requirement for designing p-TCO, so that there is no absorption of visible photons. Materials with delafossite crystal structure ABO₂ (A: monovalent ions, Cu⁺, Ag⁺; B: trivalent ions, Al⁺³, Ga⁺³, In⁺³, Cr⁺³, Fe⁺³, Co⁺³, Sc⁺³, Y⁺³, etc.) [12–14] were chosen as the candidates for p-TCOs for several reasons. Firstly, if we investigate the delafossite structure as shown in Fig. 12.2 (and discussed in details in Sect. 12.2), we see that the “pseudotetrahedral coordination (B₃AO)” with the neighboring B and A ions reduces the nonbonding nature of the oxide ions and, therefore, delocalizes the holes at the valence band edge. Secondly, this layered structure (O–A–O dumbbell layer and BO₂ layer) effectively reduces the dimension of crosslinking of A ions and, thus enlarging the bandgap [100]. And finally, another important factor in this structure is the low coordination number of the A ions, due to the large separation from oxygen ligands, which is the result of the strong coulombic repulsion between 2p electrons in oxygen ligands and A-d¹⁰ electrons. This leads to the A-d¹⁰ energy levels almost comparable to the O 2p level, resulting in a high degree of mixing of these levels, which is essential for CMVB technique [119].

The cause of p-type conductivity shown by p-TCO materials is due to excess oxygen (or metal deficit) within the crystallite sites of the material, i.e., the defect chemistry plays an important role. This deviation from the stoichiometric composition of the components can be induced by regulating the preparation condition of the materials. The defect reaction for a delafossite material of the form A^IB^{III}O₂ may be represented by the following equation [60, 184]



where “O_O” denotes the lattice oxygen, “V” denotes the vacancies of monovalent cation A^I and trivalent cation B^{III}, respectively, and “h” denotes the hole. Superscripts x, –, and + denote effective neutral, negative, and positive charge states, respectively. The symbol ↓ denotes the dissolution of oxygen within the material during oxidation.

Also, intercalation of excess O^{–2} ions in the interstitial sites may trap electrons, leaving behind empty states in the valence band, which act as holes. The formula for oxygen-excess delafossite films may be written as A^IB^{III}O_{2+x} (A^I = Cu⁺, Ag⁺ and B^{III} = Al⁺³, Ga⁺³, In⁺³, Y⁺³, Sc⁺³ cations, etc.). The value of x, i.e., the percentage of excess oxygen, may be as low as 0.001% in CuAlO_{2+x} thin film [56] to more than 25% in CuYO_{2+x} polycrystalline powder and CuScO_{2+x} thin films [128, 185–187]. Figure 12.35 shows schematic representation of nonstoichiometric ABO₂ crystal with “excess” oxygen in lattice sites and interstitial sites. Figures 12.14, 12.36, and 12.37 show some experimental evidences in support of the theory of enhanced p-type conductivity due to excess oxygen.

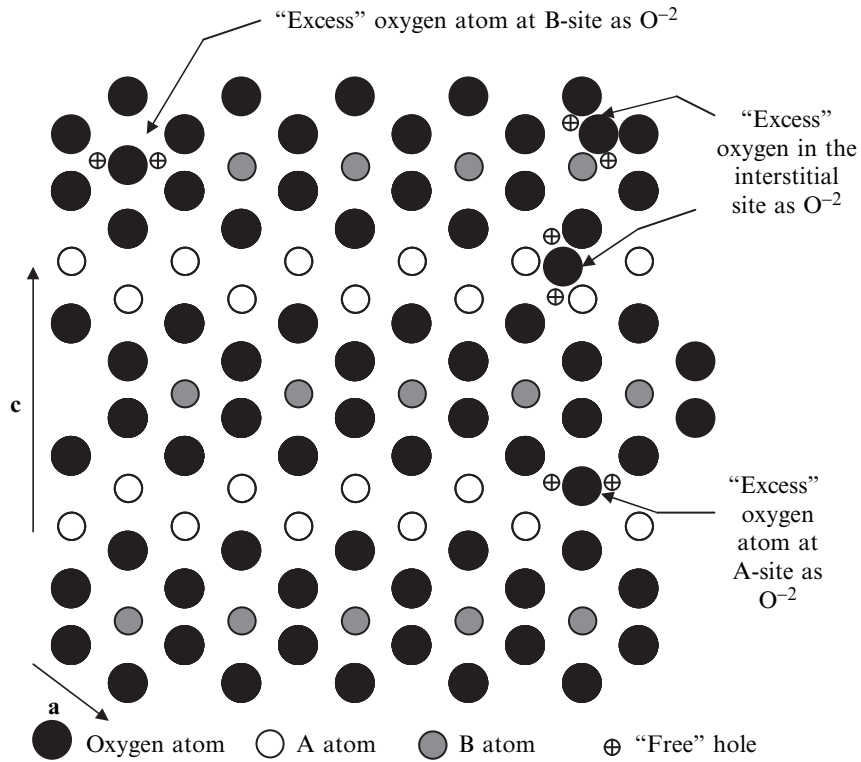


Fig. 12.35. Nonstoichiometric ABO_2 structure with "excess" oxygen in lattice sites and interstitial sites

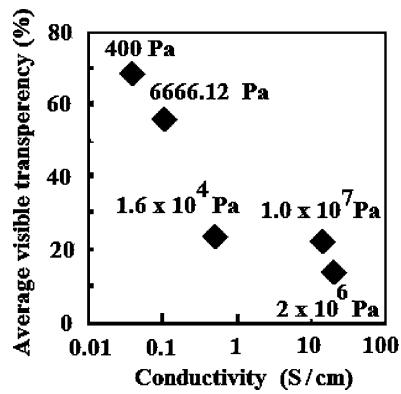


Fig. 12.36. Evidence for the increase in conductivity of $CuScO_{2+x}:Mg$ thin films for different postannealing O_2 pressure. Increase in conductivity leads to decrease in the transparency of the films (after [119])

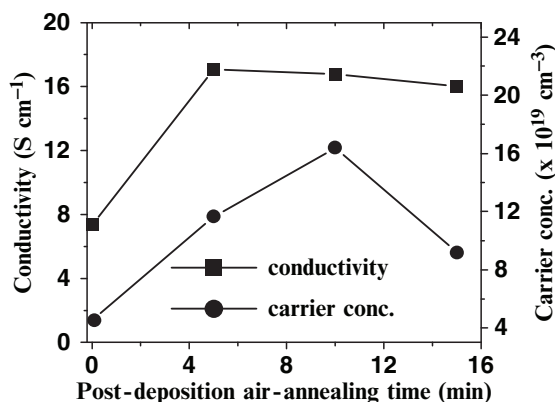


Fig. 12.37. Increase in conductivity of Cu–Al–O thin films with increase in annealing time. Evidence in support of enhanced p-type conduction is due to excess oxygen (after [150, 151])

Oxygen intercalation in delafossite p-TCOs only showed a maximum reported conductivity around $3 \times 10^1 \text{ S cm}^{-1}$ [120]. But this is still quite less than that of commercially available n-TCOs like ITO, which is having room temperature conductivity more than $1 \times 10^3 \text{ S cm}^{-1}$. So next attention was focused on the substitutional doping of these materials by appropriate dopants to increase the conductivity. Doping of CuAlO_2 was first attempted, as it was the first reported material amongst p-TCOs. Several groups theoretically calculated the effects on the electronic behavior of the material due to the presence of various cations in Cu and/or Al sites. Lalić et al. [188–190] showed that Cd and Zn substitutions on Cu site would produce n-type conductivity in the material, whereas Ni doping in Cu sites would enhance the p-type conductivity of the material. But Cd doping on Al sites would have no effect on the electrical properties of the material. Preparation of a solid solution of gallium-doped copper aluminum oxide in the form of $\text{CuAl}_{1-x}\text{Ga}_x\text{O}_2$ ($0 \leq x \leq 0.5$) was reported by Shahriari et al. [191]. But no film preparation of this material was reported by them. Also, no other experimental data on the doping of CuAlO_2 thin film has yet been reported. Heavy doping ($\sim 50\%$) of CuGaO_2 by Fe^{+3} in Ga sites has been reported by Tate et al. [119]. Their strategy was to combine high transparency of CuGaO_2 thin film ($\sim 80\%$ in visible region [111]) with better conductivity (over other Cu- and Ag-based delafossites [12–14]) of CuFeO_2 pellets (2.0 S cm^{-1} [12–14, 192]). Both the polycrystalline powder and thin film of $\text{CuGa}_{1-x}\text{Fe}_x\text{O}_2$ ($0 \leq x \leq 1$) have shown p-type conductivity. It was observed that high Fe doping had increased the conductivity of the film from $2 \times 10^{-2} \text{ S cm}^{-1}$ (for undoped CuGaO_2 thin film) to almost 1.0 S cm^{-1} for $\text{CuGa}_{1-x}\text{Fe}_x\text{O}_2$ ($x = 0.5$) thin film, whereas transparency of the films became $\sim 60\%$ in the visible region [119]. The temperature variation of conductivity of undoped and Fe-doped CuGaO_2

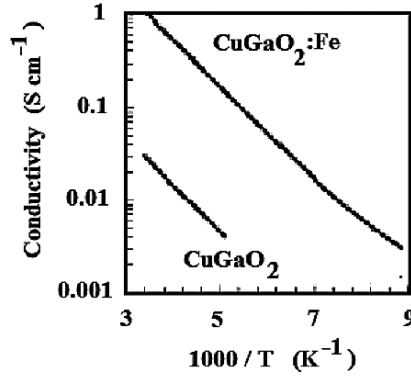
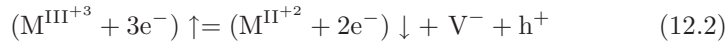


Fig. 12.38. Temperature dependence of conductivity of undoped and Fe-doped delafossite CuGaO_2 thin films, indicating increase in conductivity with doping (after [119])

thin films is shown in Fig. 12.38. Doping of CuInO_2 , CuYO_2 , CuScO_2 , and CuCrO_2 by divalent cations, e.g., Ca^{+2} , Mg^{+2} , etc., were reported by various groups [112, 113, 119–122].

When a trivalent cation was replaced by a divalent one, one empty state in the valence band was created, which acts as a hole, thus increasing hole conductivity. The method may be described by the following equation



where $\text{M}^{\text{III}+3}$ and $\text{M}^{\text{II}+2}$ are the trivalent and divalent cations, respectively, V^- is the vacant state which has been occupied by an electron e^- , and h^+ is a “free” hole. The symbols \uparrow and \downarrow denote the replacement of trivalent cation by divalent one in the lattice sites. Such doped delafossite films like $\text{CuCr}_{1-x}\text{Mg}_x\text{O}_2$ ($x = 0.05$), $\text{CuY}_{1-x}\text{Ca}_x\text{O}_2$ ($x = 0.01\text{--}0.02$), $\text{CuSc}_{1-x}\text{Mg}_x\text{O}_2$ ($x = 0.05$) showed better hole conductivity over the corresponding undoped films. The temperature variations of the aforementioned doped films are shown in Fig. 12.39.

Some Ag-based delafossite materials like $\text{AgB}^{\text{III}}\text{O}_2$ ($\text{B}^{\text{III}} = \text{Sc}^{+3}$, Cr^{+3} , Ga^{+3} , etc.) with 5% Mg doping at B^{III} sites were reported by Nagrajan et al. [128]. The conductivities of these sintered powders were very low ($\sim 10^{-5}\text{--}10^{-4} \text{ S cm}^{-1}$) and also no film preparation of these materials was reported anywhere so far.

There are also reports in the literature about the double substitution of trivalent B^{III} sites by divalent and pentavalent cations, e.g., $\text{CuFe}_{1-x}\text{V}_x\text{O}_2$ ($x = 0.5$), $\text{CuNi}_{1-x}\text{Sb}_x\text{O}_2$, $\text{CuZn}_{1-x}\text{Sb}_x\text{O}_2$, $\text{CuCo}_{1-x}\text{Sb}_x\text{O}_2$, $\text{CuMg}_{1-x}\text{Sb}_x\text{O}_2$, $\text{CuMn}_{1-x}\text{Sb}_x\text{O}_2$, $\text{AgNi}_{1-x}\text{Sb}_x\text{O}_2$, $\text{AgZn}_{1-x}\text{Sb}_x\text{O}_2$ ($x = 0.33$), etc., but all in the form of sintered powder [125, 128]. Also, triple substitution of trivalent cation had been reported by Tate and coauthors [119, 125] in the form of $\text{CuNi}_{1-x}\text{Sb}_x\text{Sn}_y\text{O}_2$ ($x = 0.3$, $y = 0.033$). Thin film of this material showed

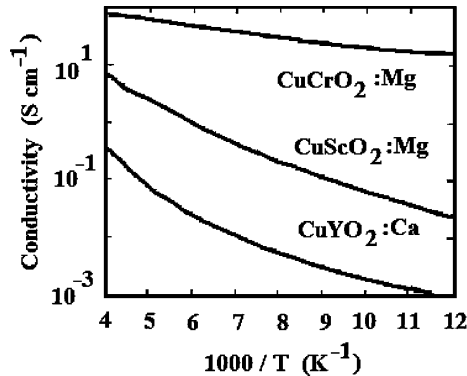


Fig. 12.39. Temperature dependence of conductivity of some doped delafossite thin films (after [121])

an average of 60% transmittance with a room temperature conductivity of $5 \times 10^{-2} \text{ S cm}^{-1}$. The exact electronic structure and conduction mechanism of these types of materials are yet to be explored completely. Tremendous opportunities are there to carry intense research work in this field.

Regarding the transparency and p-type conductivity in spinel oxide materials, the process is different than that of delafossite materials. For Ni-based spinel p-TCO films such as NiCo_2O_4 , it was found that disorder-induced small polaron hopping of holes contributes to p-type conductivity, resulting in high values of σ_{RT} , approaching 10^3 S cm^{-1} at the expense of some transparency in the visible region [52, 103]. These compositions were developed as infrared TCO materials. For Zn- d^6 transition metal oxide-based spinel materials, the low-spin ground state of transition metal oxides with d^6 configuration (such as Co, Rh, Ir), under octahedral crystal environment, behaves like Cu- d^{10} closed shell configuration, and therefore leads to p-type conductivity and optical transparency [54, 55], similar to delafossite materials. The ligand field splitting of $M-d^6$ ($M = \text{Co}^{+3}, \text{Rh}^{+3}, \text{Ir}^{+3}$) due to octahedral surroundings of sixfold oxygen ions leads to the enhancement of the bandgap of these materials [5, 54, 55]. Tremendous opportunities lie ahead to explore new kinds of spinel p-TCO materials using various models and theories.

12.6 Reactive DC Sputter Deposition of Delafossite p-CuAlO_{2+x} Thin Film

12.6.1 Introduction

As discussed in the previous sections, p-TCO thin films are very important materials in the field of optoelectronic device technology for the realization of “Transparent Electronics” [56]. Besides delafossite- and spinel-based p-TCO

thin films, mentioned in the earlier sections, some other types of p-TCO films also exist, such as undoped and K-doped SrCu_2O_2 [193, 194], oxysulfides like $(\text{LaO})\text{CuS}/\text{Se}$ [195, 196], mixed oxide like $\text{In}_2\text{O}_3-\text{Ag}_2\text{O}$ [197], and binary oxides such as NiO [198], p-type ZnO [199–203], etc. These p-TCO films have been reported to show very good electrical and optical properties with maximum visible transmittance around 90% for p- ZnO films [203] and maximum room temperature conductivity (σ_{RT}) as high as 140.0 S cm^{-1} for $(\text{La}_{1-x}\text{Mg}_x\text{O})\text{CuSe}$ films [204].

Copper aluminum oxide (CuAlO_2) is the first and the most important p-TCO material reported in thin film form [100], which has reasonable optical and electrical properties for diverse device applications. The reported visible transparency of this material is around 80% with a direct bandgap value of 3.5 eV, whereas the room temperature conductivity (σ_{RT}) is 0.34 S cm^{-1} with a carrier concentration $\sim 3.0 \times 10^{19} \text{ cm}^{-3}$ [138]. Although the reported transparency is quite high, but the hole concentration is one to two orders of magnitude lower than the corresponding well known and widely used n-TCO thin films, e.g., ITO, ZnO , SnO_2 , etc. Therefore, as far as technological aspects are concerned, improvement in the electrical characteristics of this material is very important along with the reproducibility with the required optoelectrical properties. We have previously reported an increase in the excess oxygen content as well as an increase in the p-type conductivity of DC sputtered CuAlO_{2+x} thin films with an increase in the postdeposition oxygen annealing time [80, 165]. Also we have reported very good thermoelectric and field-emission properties of p- CuAlO_2 thin films synthesized by DC sputtering technique [57, 63].

As far as thermoelectric properties of p- CuAlO_2 thin films are concerned, various groups reported enhanced thermoelectric properties of these films [82, 83], indicating its potential applications in thermoelectric converters. Also, regarding the field-emission studies of widegap p- CuAlO_2 films are concerned, our group has first reported the low-threshold field-emission properties of DC and reactive sputtered p- CuAlO_2 thin films [63, 164], which indicate that this material can become an interesting alternative to the conventional field emitters like carbon nanotubes (CNT), silicon carbide nanorods (SiC), diamond or diamond-like carbon films (DLC), amorphous carbon (a:C), etc. [205, 206].

In this section, we have reported the synthesis of p- CuAlO_2 thin films by reactive DC sputtering technique by our group. Also the structural, optical, electrical, and thermoelectric properties of these films are investigated with considerable attention and discussed in details. This may help in understanding the reactive sputtering process to deposit p- CuAlO_2 and similar types of p-TCO thin films and their potential application in “Transparent Electronics.”

12.6.2 Synthesis

Target Preparation

First of all, the target for reactive sputtering was done by mixing ultra pure metallic powder of Cu (99.999%) and Al (99.999%) with 1:1 atomic ratio thoroughly for 1.5 h. The mixture was then pressed within a grooved aluminum holder with appropriate hydrostatic pressure to form the required target. Negative terminal of the DC power supply was connected to the target and the substrates (Si and glass) were placed on the grounded electrode.

Film Deposition

Prior to the deposition, the chamber was evacuated by standard rotary and diffusion pumping arrangements to a base pressure of 10^{-6} mbar. Subsequently, the chamber was flushed with Ar several times and then the target was presputtered at 0.05 mbar in Ar atmosphere for 10 min to remove the contaminations, if any, present on the target surface. The target-to-substrate distance was kept at 1.8 cm whereas the sputtering voltage was 1.0 kV, with a current density around 12 mA cm^{-2} . During deposition, a mixture of Ar and O_2 was used as the sputtering gases (with 3:2 vol. ratio, respectively, controlled by mass-flow meters) and the sputtering pressure was kept at 0.2 mbar. The substrate was kept at an elevated temperature of 475 K. The details of the deposition procedure were reported elsewhere [163]. After every 2 h of deposition, the films were postannealed in the same vacuum chamber at 493 K for 1 h (at pressure 0.2 mbar) maintaining the oxygen flow. For this, the Ar flow was turned off and a corresponding proportional increase in the O_2 flow was manifested to keep the chamber pressure to a constant value of 0.2 mbar. The average film-deposition rate on Si substrate was 0.45 \AA s^{-1} where that for glass substrate was 0.34 \AA s^{-1} . Therefore for a deposition time of 4 h, the film thickness on Si substrate was around 650 nm and that on glass substrate was 500 nm, respectively.

Characterization

The deposited thin films were characterized by X-ray diffraction (XRD, Philips PW 1730/PW 1710, by $\text{CuK}\alpha$ line) to study the structural properties. UV-Vis-NIR spectrophotometer (Shimadzu-UV-3101-PC) was used to determine the optical properties. It is a double beam spectrophotometer with integrating sphere attachment for reflectance measurement within the wavelength range of 190–2,600 nm. The attachment is mainly used for measurement of both transmittance and diffuse/specular reflectance of the films. The integrating sphere equipped with photomultiplier (UV-Vis region) and PbS cell (NIR region) detectors. Both the optical transmission and reflection spectra of the films deposited on glass substrates were recorded taking similar glass

as reference, and hence the spectrum gives transmittance and reflectance of the films only. Thermoelectric power and Hall effect studies were used to determine the type of conduction taking place within the deposited films. For thermoelectric power measurement (temperature variation of Seebeck coefficient), a temperature gradient across the sample was created by keeping one end of the film in a hot-head and the other in a cold-head. The hot-head temperature was varied from room temperature to 460 K, whereas the cold-head was kept at room temperature. And these temperatures of the hot and cold ends of the film were measured by proper thermocouple arrangements. The thermo-emfs generated between the hot and cold ends of the sample, at different hot-end temperatures, were used to determine the Seebeck coefficients (S) of the material. The entire system was kept under vacuum condition. For Hall study, we have used van der Pauw method, with rectangular van der Pauw configuration. The electrical connections were made at the four corners of the sample. For the measurement of Hall voltage and related parameters, an electromagnet (Polytronic Corporation) with 4 in. pole pieces was used along with a stabilized power supply (current range 0–6 A, voltage range 0–100 V) to monitor the field strength. The distance between the pole pieces could be varied and for a separation of 3.0 cm of pole pieces, the field strength could be adjusted to a maximum of 10 kG. The field within the measuring system was determined by using Differential Gaussmeter. The sheet resistance and temperature dependence of electrical conductivity of the films were studied by linear four-probe method using Kiethley electrometer (Model – 6514) from 300 to 550 K. All the contacts were made with silver paint, which showed linear I–V characteristic over a wide range of applied voltage.

12.6.3 Results and Discussion

Structural Properties

Figure 12.40 shows the XRD spectrum of the film deposited on Si substrate with background correction. It shows a strong (006) orientation. Previous

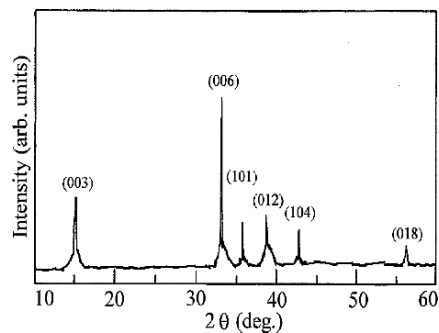


Fig. 12.40. XRD pattern of the reactive DC sputtered CuAlO_2 thin film

Table 12.13. Crystal data for CuAlO_2 [108, 114, 117, 207]

System – rhombohedral
Space group – $R\bar{3}m$ (D_{3d})
$a = 2.858 \text{ \AA} = b, c = 16.958 \text{ \AA}$
$\alpha = 28.1^\circ = \beta$
$\text{Cu-O} = 1.86 \text{ \AA}, \text{Al-O} = 1.91 \text{ \AA}, \text{Cu-Cu} = 2.86 \text{ \AA}$

Table 12.14. Comparison between the JCPDS d values [207] and observed d values of reactive sputtered CuAlO_2 thin films

$h k l$	d_{JCPDS} (\AA)	d_{reactive} (\AA)
0 0 3	5.61	5.67
0 0 6	2.82	2.79
1 0 1	2.44	2.48
0 1 2	2.376	2.374
1 0 4	2.133	2.111
1 0 7	1.732	–
0 1 8	1.612	1.618

workers [124, 138] also obtained similar orientation for CuAlO_2 films deposited by PLD method on sapphire substrate. We have also observed strong (006) orientation in our previously reported DC sputtered CuAlO_2 thin films deposited on Si substrates [143]. Along with the above peak, other peaks were also observed in the XRD spectrum which could be assigned for (003), (101), (012), (104), and (018) reflections of crystalline CuAlO_2 . Also no peaks corresponding to starting materials, e.g., Cu and Al metal powders as well as their oxides, were found in the pattern. This conclusively indicated that the reactants were properly mixed to give the proper phase of the copper aluminum oxide and no residual metal oxides remained in the film. As far as other previously reported reactive sputtered-deposited copper aluminum oxide thin films are concerned, most of the reports indicate phase impure films, which contain a mixture of CuAlO_2 , Cu_2O , CuAl_2O_4 , and CuO [158, 161, 162, 165]. Table 12.13 gives various crystal data of CuAlO_2 and Table 12.14 compares experimentally obtained d values of reactive sputtered CuAlO_2 thin film with JCPDS value [207].

The information on particle size of very small crystallites from the measured full-widths-at-half-maximum (FWHM) of the diffraction peaks can be estimated from the well-known Scherrer formula [208]

$$L = \frac{x\lambda}{\beta_1 \cos \theta}, \quad (12.3)$$

where L is the particle size, β_1 is the particle broadening of diffraction peaks measured at FWHM of the peak at a certain 2θ value, x is a correction factor

(=0.9), and λ is the wavelength of the X-ray used. It is to be mentioned here that, when the size of the individual crystallites in a polycrystalline sample is less than 100 nm, the term “particle size” is usually used [208].

In polycrystalline thin films, due to the interaction between grains of the films as well as that with the substrate, a single grain in the polycrystalline thin film is not free to deform in the same way as an isolated crystal would, if subjected to the same deforming force. As a result of this restraint by its neighbors, a deformed grain in a polycrystalline aggregate is usually in a state of tension or compression. Thus an “internal stress” or “residual stress” is generated within the films. This residual stress produces uniform or nonuniform strain within the film. If the grains are subjected to a uniform tensile strain at right angles to the X-ray reflecting planes, corresponding diffraction peaks shift to the lower angles but do not change otherwise. Similarly for uniform compressive strain, the diffraction peaks shift to the higher angles with no change otherwise. On the other hand, if the strain is nonuniform then the diffraction peak will be broadened, which is called “strain broadening” [208]. The relation between this broadening and the strain can be obtained by differentiating the Bragg’s law as follows [208]

$$\begin{aligned} 2\Delta d \sin \theta + 2d \cos \theta \Delta \theta &= 0, \\ \Rightarrow \Delta \theta &= -\frac{\Delta d}{d} \tan \theta, \\ \Rightarrow \Delta(2\theta) &= -2\varepsilon \tan \theta, [\Delta d/d = \varepsilon], \\ \Rightarrow \Delta\beta &= -2\varepsilon \tan \theta, [\beta = 2\theta], \end{aligned} \quad (12.4)$$

where $\Delta\beta$ is the extra broadening of the diffraction peaks over and above the instrumental breadth (therefore also called “instrumental broadening”), ε is the strain generated within the films, and θ is the Bragg angle. Now the above equation contains both tensile and compressive strain and must be divided by two to obtain maximum tensile strain alone or maximum compressive strain alone, if these two are assumed equal. Hence, the equation for strain broadening for only one type of strain will be

$$\Delta\beta = -\varepsilon \tan \theta. \quad (12.5)$$

Now if both the effect of “particle-size broadening” and “strain broadening” is taken into consideration, then the total broadening (β) can be expressed as a linear combination of (12.3) and (12.5) as follows [208]

$$\begin{aligned} \beta &= \beta_1 + |\Delta\beta| = \frac{\lambda}{L \cos \theta} + \varepsilon \tan \theta \\ \Rightarrow \frac{\beta \cos \theta}{\lambda} &= \frac{1}{L} + \frac{\varepsilon \sin \theta}{\lambda}, \end{aligned} \quad (12.6)$$

where β is the FWHM of the observed peaks, L is the effective particle size, and ε is the effective strain. A plot of $\beta \cos \theta / \lambda$ vs. $\sin \theta / \lambda$ will be a straight

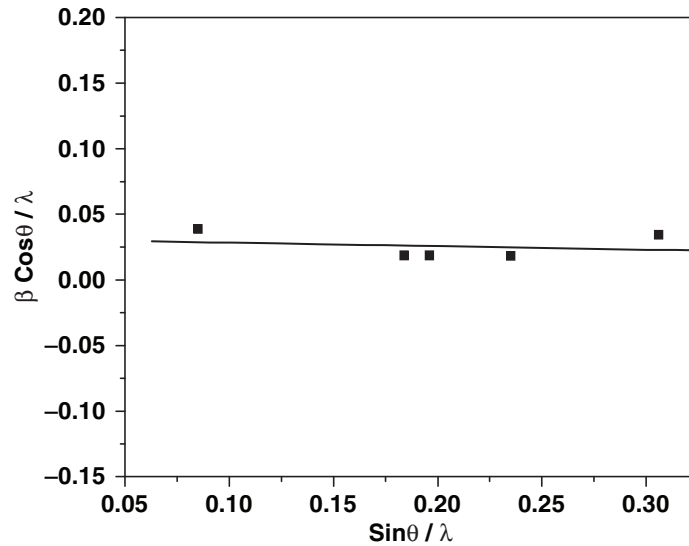


Fig. 12.41. Determination of strain and particle size of CuAlO_2 film deposited by reactive sputtering

line, slope of which will give the estimation of the effective strain, whereas the intercept on $\beta \cos\theta/\lambda$ -axis will carry the information of the effective particle size.

Figure 12.41 represents the plot of $\beta \cos\theta/\lambda$ vs. $\sin\theta/\lambda$, obtained from the XRD pattern of the CuAlO_2 thin film deposited by reactive sputtering on Si substrate (shown in Fig. 12.40). Slope of the graph depicts the strain value as 2.70×10^{-2} and the intercept on y -axis gives the particle size as ~ 32 nm.

Compositional Analyses

Composition analyses were done by A Leica S-440 Oxford ISIS Energy Dispersive X-Ray (EDX) instrument. The instrument has the capability to detect elements from Boron (5) to Uranium (92) with less than 5% accuracy. In reactive DC sputtering method, films were postannealed for 60 min in oxygen atmosphere and the composition of the film was in the ratio of $\text{Cu:Al:O} = 1:1:2.08$. Therefore, the chemical formula of the films may be written as $\text{CuAlO}_{2.08}$. This means that the percentage of excess oxygen in the reactive sputtered films is around 4 at.%. It has been observed that the percentage of excess oxygen within the reactive sputtered films is close to that of DC sputtered films with $t_a = 90$ min [144].

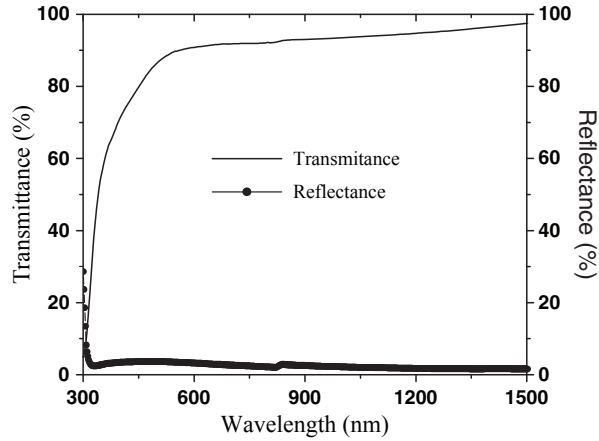


Fig. 12.42. UV-Vis-NIR spectra of reactive DC sputtered CuAlO_2 thin film

UV-Vis-NIR Measurements

Optical properties of CuAlO_2 thin films are extremely important because of its possible applications in the field of optoelectronics technology. High transparency coupled with high conductivity is the main feature for TCOs as mentioned earlier. Therefore, detailed optical characterization and determination of related parameters are the most significant part of the analyses of TCOs. Following this point of view, we have studied the optical properties of reactive sputtered CuAlO_2 thin films in details. The films were deposited on glass substrates and the film thicknesses were measured around 500 nm from cross-sectional SEM (not shown here). Figure 12.42 shows the UV-Vis-NIR spectra of reactive DC sputtered CuAlO_2 thin film in the wavelength range of 300–1,500 nm. These films were postannealed for 60 min. The average visible transmittance of the film is found to be $\sim 85\text{--}90\%$.

Now, we have critically analyzed the variations of transmittance (T) and reflectance (R) in terms of absorption coefficients (α) to derive information on the optical transitions occurring in these films. The transmittance (T), reflectance (R), and absorption coefficient (α) of a specimen are related by the equation [209]

$$T = \frac{(1 - R)^2 e^{-\alpha d}}{1 - R^2 e^{-2\alpha d}}, \quad (12.7)$$

where d is the film thickness and here the multiple internal reflections within the film are considered. Now at the region of fundamental absorption, α will be quite high, so also αd . So we can neglect the second term of the denominator of (12.7) and rewrite it as [209, 210]

$$T \approx (1 - R)^2 e^{-\alpha d}. \quad (12.8)$$

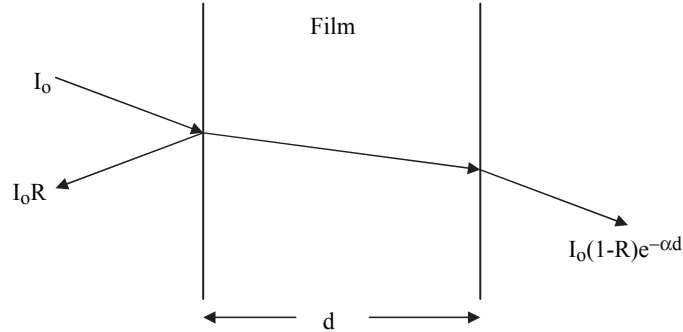


Fig. 12.43. Incident (I_0), reflected ($I_0 R$), and transmitted [$I_0(1 - R)e^{-\alpha d}$] rays in a thin film of thickness d . Multiple internal reflections are neglected

Knowing T , R , and d , absorption coefficients can be determined. If R is not known, then from transmittance data of two samples of known thicknesses d_1 and d_2 , α can be obtained from the relation [209]

$$\frac{T_1}{T_2} \approx e^{\alpha(d_2 - d_1)}. \quad (12.9)$$

Beyond the absorption edge if one can observe the interference effect in the transmittance and reflectance spectra due to the multiple internal reflections within the film, then it will be possible to find the refractive index (n) of the material by measuring the wavelengths (λ_1 and λ_2) at two adjacent maxima. The expression will be [209]

$$n = \frac{\lambda_1 \lambda_2}{|\lambda_1 - \lambda_2|}. \quad (12.10)$$

Now, according to the schematic diagram shown in Fig. 12.43, in the spectral region of fundamental absorption, as a first approximation, T , R , and α will be related by the following equation [211] (here, we have neglected the internal multiple reflections for TCOs, unlike (12.7) and (12.8))

$$T \approx (1 - R)e^{-\alpha d} \quad (12.11)$$

and

$$R = \frac{(n - 1)^2 + k^2}{(n + 1)^2 + k^2}, \quad (12.12)$$

where n is the refractive index and k is the extinction coefficient, which is related to the wavelength (λ) and absorption coefficient (α) by the following equation:

$$k = \frac{\lambda \alpha}{4\pi}. \quad (12.13)$$

Now, for transparent medium (as in our p-CuAlO₂ films), $k^2 \ll (n - 1)^2$ and (12.12) will be reduced to

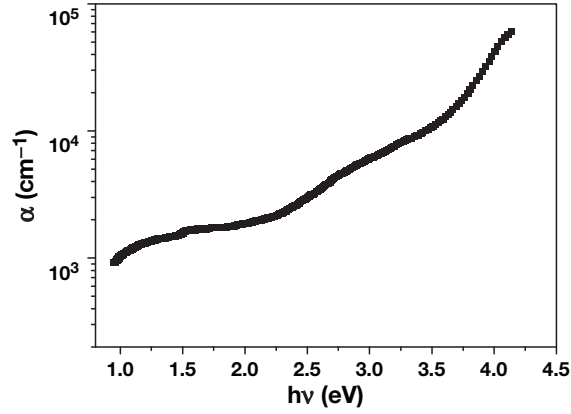


Fig. 12.44. Energy dependence of absorption coefficients

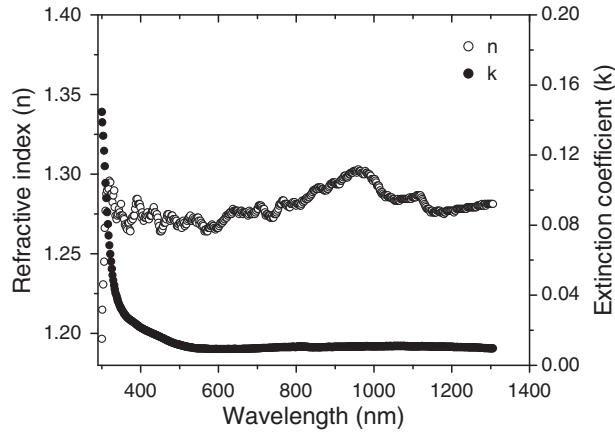


Fig. 12.45. Spectral variation of extinction coefficients and refractive indices of reactive sputtered CuAlO₂ film

$$n = \frac{1 + \sqrt{R}}{1 - \sqrt{R}} \tag{12.14}$$

and the absorption coefficients (α) can be calculated by rewriting (12.11) as

$$\alpha = \frac{1}{d} \ln \left[\frac{1 - R}{T} \right]. \tag{12.15}$$

The spectral variations of α , n , and k are shown in Figs. 12.44 and 12.45. It has been observed that the refractive index varies between 1.2 and 1.3 in the wavelength range of 300–1,300 nm. Although there are no reported data on the refractive indices of CuAlO₂ thin film, but these data are reasonable when compared with other TCOs such as ITO (1.75–2.0 in the wavelength

range of 400–1,200 nm [212]) and CdO (1.31–2.84 in the wavelength range of 500–2,500 nm [213]).

In the range of the onset of absorption edge, the absorption coefficients (α) can be described by the relation for parabolic bands, i.e., [209, 210]

$$(\alpha h\nu)^{1/n} = A(h\nu - E_g), \quad (12.16)$$

where E_g is the bandgap of the material, the exponent n depends on the type of transition. For direct allowed transition, $n = 1/2$; for indirect allowed transition, $n = 2$; and for direct forbidden transition, $n = 3/2$.

The factor A also depends on the type of transition.

For direct allowed transition,

$$A \approx \frac{e^2 \left(2 \frac{m_h^* m_e^*}{m_h^* + m_e^*} \right)^{3/2}}{nch^2 m_e^*};$$

for direct forbidden transition,

$$A = \frac{4}{3} \frac{e^2 \left(\frac{m_h^* m_e^*}{m_h^* + m_e^*} \right)^{5/2}}{nch^2 m_e^* m_h^* h\nu};$$

and for indirect allowed transition,

$$A \propto \frac{(m_h^* m_e^*)^{3/2}}{\pi^4 h^6},$$

where n is the refractive index of the material, m_h^* and m_e^* are the effective masses of holes and electrons, respectively) [214].

To determine the possible transitions, $(\alpha h\nu)^{1/n}$ vs. $h\nu$ were plotted for different values of n . The $(\alpha h\nu)^2$ vs. $h\nu$ and $(\alpha h\nu)^{1/2}$ vs. $h\nu$ plots for reactive sputtered-deposited CuAlO₂ thin film are shown in Fig. 12.46. Extrapolating the linear portion of the graphs to the $h\nu$ -axis, we have obtained the direct and indirect bandgaps as ~ 3.90 and 1.89 eV, respectively. These values are comparable to those reported previously by Kawazoe et al. (3.5 eV) [100] and Yanagi et al. (3.5 and 1.8 eV) [116] for their pulsed laser-deposited CuAlO₂ thin films and also fall in the range theoretically calculated by Robertson et al. (3.91 and 2.1 eV) [117]. Also Stauber et al. [138] obtained the direct bandgap of their RF sputter-deposited CuAlO₂ thin film around 3.5 eV, whereas Wang and Gong [150, 151] reported the direct bandgap of their plasma-enhanced chemical vapor-deposited (PECVD) copper aluminum oxide films around 3.6–3.75 eV. As far as the bandgap values of reactive sputtered copper aluminum oxide films synthesized by other groups are concerned, Ong and Gong [158] reported these values around 2.9–3.3 eV, Yang et al. [139] around 3.81 eV, Reddy and coauthors [165] around 3.54 eV, and Tsuboi et al. [161, 162] around 3.5 eV. These values are slightly less than that of our value, which is mainly because of their phase impure films, which contain some amount of CuO, Cu₂O, and/or CuAl₂O₄ phases within the copper aluminum oxide samples.

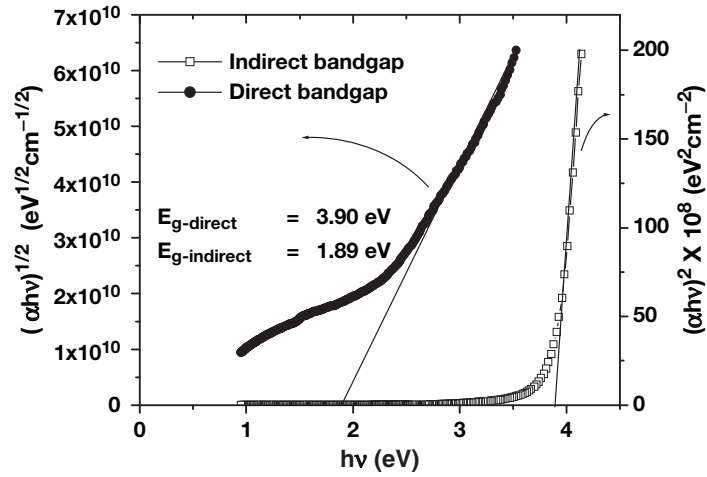


Fig. 12.46. Determination of bandgaps of reactive sputtered CuAlO₂ film

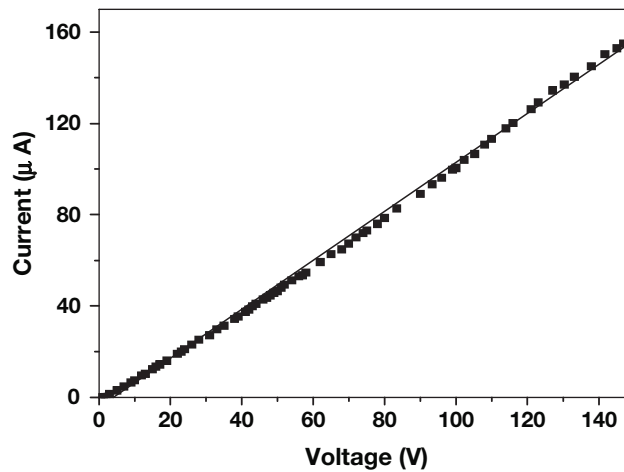


Fig. 12.47. Verification of ohmic nature of the contacts

Electrical Properties

Electrical properties of CuAlO₂ thin films have been studied by standard four-probe methods. All electrical contacts were made by silver paint, which showed linear I-V characteristics over a wide range of voltages and temperatures. Figure 12.47 shows I-V characteristics of one contact at room temperature indicating ohmic nature of it over the voltage range up to 150 V.

The thermally activated conduction of a semiconductor can be given by the relation [135]

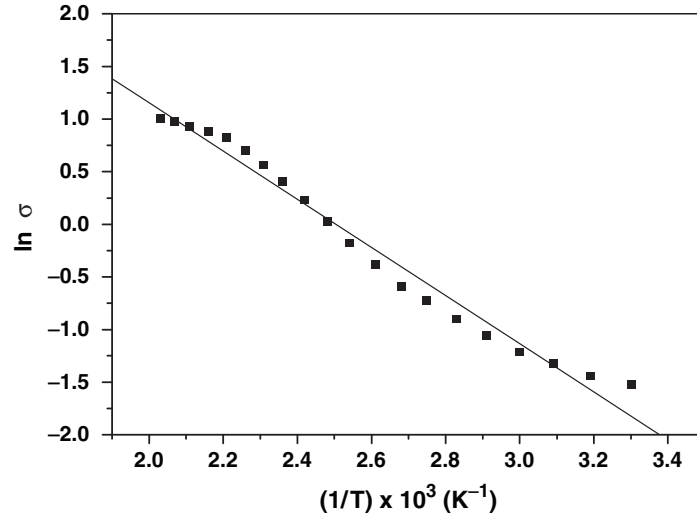


Fig. 12.48. Temperature variation of conductivity of reactive sputtered CuAlO_2 thin film

$$\sigma = \sigma_0 \exp \left[-\frac{E_a}{kT} \right], \quad (12.17)$$

where σ_0 is a temperature-independent factor and E_a is the activation energy of the material. For p-type semiconductor (as in our p- CuAlO_2 sample), this is the energy difference between the acceptor level and the top of the valence band. Therefore, a plot of $\ln \sigma$ vs. $1/T$ should be a straight line whose slope would carry the information of the activation energy of the material. Temperature variation of the conductivity of reactive sputtered CuAlO_2 thin film has been studied in the temperature range of 300–550 K according to (12.17) and shown in Fig. 12.48. The film thickness was ~ 500 nm obtained from cross-sectional SEM (not shown here). The temperature variation of conductivity of the CuAlO_2 thin films was studied below the room temperature by previous authors [100,116], but no study on high-temperature conduction was reported. The straight line nature of the Arrhenius plot indicates the thermally activated conduction as often found in semiconductors. Room temperature conductivity (σ_{RT}) of the film was obtained as 0.22 S cm^{-1} , which is comparable to that obtained by DC sputtered films postannealed for 60 min [143]. From the slope of the graph, we get the value of activation energy (E_a) which corresponds to the minimum energy required to transfer carriers from acceptor level to the valence band and the value of E_a comes out as 250 meV, which is comparable to that of DC sputtered films postannealed for 60 min [57]. For other reactive sputtered CuAlO_2 films, Rao et al. [165] obtained σ_{RT} around 0.36 S cm^{-1} . On the other hand, Tsuboi et al. [161,162] reported the resistivity of their reactive cosputtered Cu–Al–O thin film around $10\text{--}10^2 \Omega \text{ cm}$.

Hall measurements of our reactive sputtered films were done at room temperature. Hall coefficient of the film was determined to be $R_H = 14.1 \text{ cm}^{-3} \text{ C}^{-1}$, corresponding to carrier density $4.4 \times 10^{17} \text{ cm}^{-3}$. Positive value of Hall coefficient confirmed the p-type conductivity of the film. The carrier concentration of this film is comparable to that of DC sputtered film postannealed for 60 min [57]. As far as conductivities of previously reported reactive sputtered copper aluminum oxide films are concerned, Rao and coauthors [165] obtained the Hall mobility and hole concentration as $13.1 \text{ cm}^2 \text{ V}^{-1} \text{ S}^{-1}$ and $1.5 \times 10^{17} \text{ cm}^{-3}$, respectively.

Thermoelectric Properties

Thermoelectric properties of reactive sputtered CuAlO_2 thin films have been studied for films deposited on glass substrates. The measurements were done from room temperature (300 K) to 550 K. Figure 12.49 shows the temperature dependence of Seebeck coefficients (S) of the film. All the Seebeck coefficients are positive in nature, which again confirmed p-type nature of the films. Room temperature Seebeck coefficient (S_{RT}) of the film was obtained as $+115 \mu\text{V K}^{-1}$. As shown in the Fig. 12.49, the Seebeck coefficients initially decrease from room temperature to around 370 K and then increase to almost $+520 \mu\text{V K}^{-1}$, for further increase in temperature. Previously, Kawazoe et al. [100] and Yanagi et al. [116] obtained the room temperature Seebeck coefficients for their pulsed laser-deposited CuAlO_2 thin film as $+183$ and $+214 \mu\text{V K}^{-1}$, respectively, which is comparable to our values. On the other hand, Koumoto et al. [60] determined the Seebeck coefficient of CuAlO_2 single crystal as well as polycrystal at 600 K around $+180$ and $+150 \mu\text{V K}^{-1}$, respectively. Also Benko and Koffyberg [107] reported a relatively high value of S_{RT} ($670 \mu\text{V K}^{-1}$) of CuAlO_2 powdered pellets. As far as

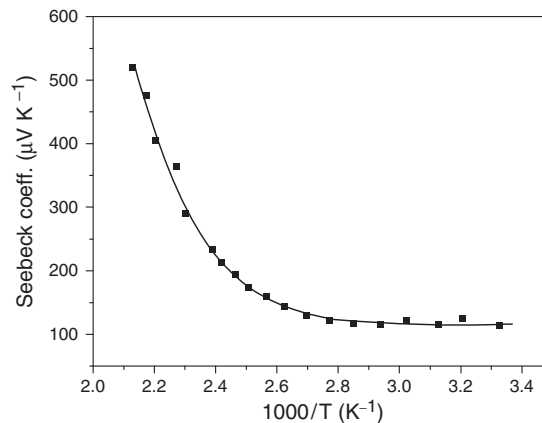


Fig. 12.49. Seebeck coefficient vs. $1,000/T$ of reactive sputtered CuAlO_2 thin films

reactive sputtered p-CuAlO₂ thin films are concerned, nobody has mentioned about the Seebeck coefficient of those films, but various groups have reported enhanced thermoelectric properties of CuAlO₂ as well as similar delafossite materials [80–83] synthesized by various other techniques, which indicate that this type of material may become very good alternative to the commercially available thermoelectric converters.

It has been observed that, in our reactive sputter-deposited CuAlO₂ thin film, S_{RT} increases with the increase in conductivity of the films. This observation is consistent with the Hicks model [215, 216], where the natural superlattice structure was proposed to show high thermoelectric figure of merit (ZT) due to increase in both S and σ according to the following equation

$$ZT = \frac{S^2 \sigma T}{\kappa}, \quad (12.18)$$

where σ is the electrical conductivity, κ is the thermal conductivity, and S is the Seebeck coefficient.

To achieve high ZT , increase in S and/or σ and decrease in κ are required. But for simple materials, increase in S leads to a decrease in σ . Similarly, an increase in σ is followed by an increase in κ according to Wiedemann–Franz law. So ZT effectively remains more or less constant. To increase Z , various models have been proposed in the last decade. Amongst them, the most exciting proposal by Hicks et al. [215, 216] was superlattice quantum-well materials, having an effective two-dimensional density of states for carriers. This density of state is given by $m/\pi\hbar^2a$, where m is the carrier mass and a is the quantum-well width. These authors assumed infinite potential barrier with zero barrier width and showed a considerable increase in Z . Later, Lin-Chung and Reinecke [217] and Broido and Reinecke [218] included the effects of thermal transport in the finite barrier layers and carrier tunneling between layers in the above model to get a modified Z . Encouraged by these findings, various new materials, having layered structure, have been investigated in the last few years, which include NaCo₂O₄ [219], (ZnO)₅In₂O₃ [220], PdCoO₂ [58], CuAlO₂ [59, 60], etc.

Structure of CuAlO₂ delafossite has been shown in Fig. 12.2 and described in details in previous sections. This structure suggests that CuAlO₂ has a layered structure where carriers can easily move two dimensionally along ab -plane than to move across the Al–O insulating layers (described in Fig. 12.50). In the XRD pattern of our CuAlO₂ thin film (shown in Fig. 12.40), we have obtained a strong (006) peak, which is typical of a texture where the c -axis is perpendicular to the substrate (hence parallel to the normal, n to the substrate, i.e., $c \parallel n$). Now, according to our experimental setup (as described earlier), carriers in the films are expected to move along the ab -plane. Hence, the above argument of two-dimensional confinement of carriers along the ab -plane is valid for our films. Although the reason behind the enhanced thermoelectric properties shown by the materials possessing layered structure is still not fully understood, but Koumoto et al. [60] suggested that

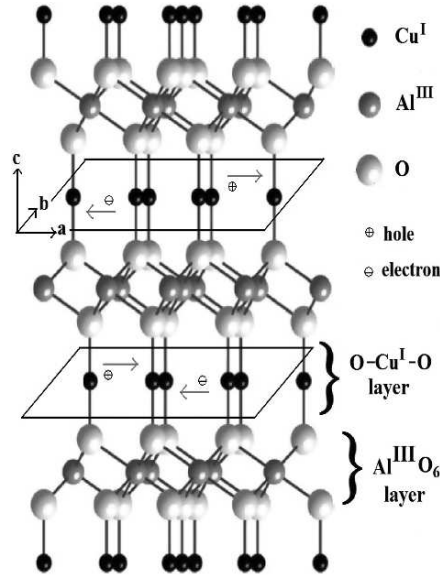


Fig. 12.50. Layered structure of CuAlO_2 showing the carriers confined in the ab -plane

this may be correlated with the low dimensionality of the crystal structure and behavior of electrons and phonons in an anisotropic structural environment. Recently, Wang et al. [221] suggested that spin entropy might be responsible for enhanced thermopower in $\text{Na}_x\text{Co}_2\text{O}_4$ having layered structure [219]. Whether this can be correlated with the good thermoelectric properties of CuAlO_2 is a question and intense research is needed in this direction.

The variation of thermoelectric power (S) with temperature is given by [222]

$$S = \frac{k}{e} \left(A + \frac{\Delta E_f}{kT} \right) \tag{12.19}$$

with

$$A = \frac{5}{2} - s \tag{12.20}$$

and

$$\tau = \tau_0 e^{-s}, \tag{12.21}$$

where k is the Boltzmann constant, e is the electronic charge, ΔE_f is the energy difference between Fermi level and the upper edge of the valence band, τ is the relaxation time for electron scattering, s is a constant, which is different for different scattering mechanism, and τ_0 is a constant, which is a function of temperature but independent of the electronic charge, e .

From (12.19), we can obtain the Fermi level (E_f), from the slope of the S vs. $1/T$ graph. From Fig. 12.49, we have determined the Fermi energy from the linear portion of the graphs near room temperature, and the value obtained as 100 meV. Previously, Benko and Koffyberg [107] have determined the Fermi energy of CuAlO_2 powder ($\sigma = 1.69 \times 10^{-3} \text{ S cm}^{-1}$) from the thermopower measurement, as 190 meV, which is slightly higher to our sample. This is mainly because we have measured the thermopower of the material as thin film form, whereas they had done their measurements on polycrystal pellets. As previously mentioned, from the slope of the $\ln \sigma$ vs. $1,000/T$ plots (Fig. 12.48), we have obtained the activation energy ($E_a = 250 \text{ meV}$) value of our sample, which gives the estimation of acceptor levels. Comparing this value with the Fermi energy of the material, we can say that, according to the band picture, Fermi level lies between the upper edge of the valence band and the acceptor level, which is typical of a nondegenerate p-type semiconducting material with acceptors not fully ionized. Hence a continuous increase in conductivity with temperature was observed for our sample. The values of various optical, electrical, and thermoelectric parameters of the reactive sputtered CuAlO_2 thin films are furnished in Table 12.15. Figure 12.51 represents the temperature dependence of thermoelectric power factor (σS^2) of CuAlO_2 thin film for the temperature range of 300–460 K. The values range from $3.09 \times 10^{-7} \text{ W m}^{-1} \text{ K}^{-2}$ at temperature around 300 K to $5.5 \times 10^{-5} \text{ W m}^{-1} \text{ K}^{-2}$ around 460 K. Previously, Koumoto et al. [60] obtained these values roughly as $1.12 \times 10^{-5} \text{ W m}^{-1} \text{ K}^{-2}$ at 550 K for CuAlO_2 single crystal and $7.1 \times 10^{-6} \text{ W m}^{-1} \text{ K}^{-2}$ at 700 K for CuAlO_2 polycrystal. Also Park et al. [59] obtained the power factor for CuAlO_2 ceramic as $2 \times 10^{-5} \text{ W m}^{-1} \text{ K}^{-2}$ at 550 K. These values are comparable to the values reported by us. Also, recently Kurotori and Sugihara [223] reported significant increase in the thermoelectric properties of CuAlO_2 , when doped with Zn and Ca. All these reports suggest that this class of material may become very good candidate of thermoelectric converter, and may bring renaissance in the thermopower industry.

In summary, highly transparent, p-type semiconducting CuAlO_2 thin films have been synthesized by reactive sputtering technique. The film with thickness $\sim 500 \text{ nm}$ shows almost 80–85% visible transmittance with 0.22 S cm^{-1} room temperature conductivity. Hall measurements confirmed p-type conductivity with a hole concentration $\sim 4.4 \times 10^{17} \text{ cm}^{-3}$. These results indicate that reactive sputtering can become a very good, cost-effective, large-scale synthesis procedure to fabricate p-TCO films with enhanced electro-optical properties for potential applications in “Invisible Electronics” as well as in other diverse device technologies. The film also showed very good thermoelectric properties indicating its possible use in thermoelectric industries.

Table 12.15. Different thermoelectric properties of reactive sputtered p-CuAlO₂ thin film

Thickness (nm)	Average visible transparency (%)	E_g -direct (eV)	E_g -indirect (eV)	σ_{RT} (S cm ⁻¹)	E_a (meV)	n (cm ⁻³)	R_H (cm ⁻³ C ⁻¹)	S_{RT} (μ V K ⁻¹)	E_f (meV)
500	80–85	3.90	1.89	0.22	250	4.4×10^{17}	14.1	+115	100

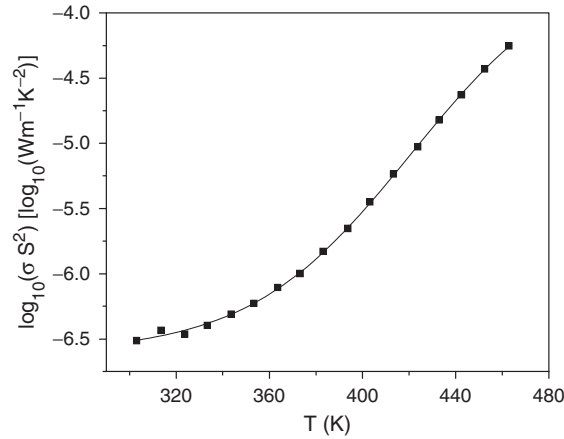


Fig. 12.51. Thermoelectric power factor vs. temperature of reactive sputtered CuAlO₂ thin films

12.7 Conclusions and Future Directions

12.7.1 Conclusions

Reactive sputtering technique has become one of the interesting and widely used deposition techniques to fabricate binary, ternary, and quaternary metal oxide thin films which are having many useful applications in optoelectronics as well as in various other technological fields. Being a cost-effective procedure, this thin film-deposition process has the capability of large-scale production in diverse industrial applications. In this chapter, we have briefly discussed various aspects of reactive sputtering technique and its applications in the field of p-TCO thin films, especially spinel, AB₂O₄, and delafossite, and ABO₂ thin films, which are having tremendous applications in “Transparent” or “Invisible Electronics.”

Spinel- and delafossite-structured, transparent, p-type semiconducting oxide (p-TCO) materials are recently gained renewed interest in the field of optoelectronics technology for the possible fabrication of all-transparent junctional devices which can be used as a “functional” window that would transmit the visible portion of the solar spectrum but absorb the ultraviolet part of it to generate electricity. Here we have reviewed in details the recent developments in the spinel- and delafossite-structured p-TCO materials. Various deposition techniques used to synthesize these types of materials are discussed and especially different reactive sputtering techniques used to synthesize spinel and delafossite p-TCO films are compared in details. It has been observed that the reactive sputtering of elemental targets in oxygen-diluted argon atmosphere produced dense sputtering plasma, leading to uniform and good quality films.

Also, the origin of the p-type conductivity in these spinel and delafossite oxide films is discussed in details. Nature of the cationic species, crystal structure of the material, and nonstoichiometry are found to be playing important roles in the hole conductivity of these materials. Metal deficit or excess oxygen within the material is found to increase the p-type conductivity of these materials. Postdeposition oxygen annealing of the films as well as excess oxygen atmosphere during film deposition are found to be responsible for the presence of those nonstoichiometric excess oxygen within the films.

Finally, a detailed discussion on the synthesis and characterization of polycrystalline, p-type semiconducting, transparent, delafossite, and wide-bandgap CuAlO_2 thin films by reactive DC sputtering technique has been presented. CuAlO_2 , being the first reported p-TCO in thin film form, found to be one of the very important materials in the field of "Transparent Electronics." The films were deposited by reactive sputtering of a target pellet composed of Cu + Al (1:1 atomic ratio) metal powders in Ar + O₂ (3:2 vol. ratio) atmosphere under elevated substrate temperature. XRD spectrum confirms the polycrystalline nature of the films with small grain size (~ 32 nm). The deposited films were highly transparent in the visible region with direct and indirect bandgap values of 3.90 and 1.89 eV, respectively. p-Type conductivity was confirmed from both thermoelectric power and Hall effect measurements. Reactive sputtered-deposited transparent p-type semiconducting CuAlO_2 thin film showed fairly high conductivity with maximum room temperature conductivity in the range of 0.22 S cm^{-1} and a carrier concentration $\sim 4.4 \times 10^{17} \text{ cm}^{-3}$. Also the activation energy of the film is found to be 250 meV. Compositional analyses reveal the presence of excess oxygen within the film with a chemical formula $\text{CuAlO}_{2.08}$. FT-IR spectra of the films indicated the existence of various bondings among Cu, Al, and oxygen. Thermopower measurements indicate that CuAlO_2 may become a candidate material for thermoelectric conversion. CuAlO_2 has a natural superlattice structure, with an effective two-dimensional density of states (along *ab*-plane). This type of layered-structure material could become a good thermoelectric material. Room temperature Seebeck coefficients (S_{RT}) are found to be $+115 \mu \text{ V K}^{-1}$ with $E_{\text{f}} = 100 \text{ meV}$. An increase in S_{RT} with σ_{RT} is observed, which is expected for superlattice materials. The cost-effective fabrication of this technologically important material is extremely important for the large-scale production of device quality films. Low-cost physical routes like reactive sputtering technique will enable fabrication of high-quality films for diverse device applications.

12.7.2 Future Directions

First and foremost future course of the research will be to increase the conductivity of these p-TCO materials. The maximum conductivity of our p-TCO films with spinel and delafossite structure is almost two orders of magnitude less than that of commercially available n-TCO films. So this may put hin-

drance in the formation of effective active devices for large-scale production. It is found that nonstoichiometric oxygen intercalation within the material has its limitation to increase the conductivity of the film. Excess oxygen intercalation, beyond an optimum value, is found to deteriorate the film quality. So intentional doping of the material is the obvious step to increase the conductivity of the film. Identification of proper dopant and doping procedure should be the focus of the future work to deposit superior device quality films for the development of “Transparent Electronics.”

Another interesting area of research is the cost-effective fabrication of transparent junctions, without compromising its electro-optical properties. This is important for the large-scale production of various junctional devices with diverse applications. Several groups have used various cost-effective physical and chemical routes for fabrication of transparent junctions, but future work should be aimed to improve the optoelectrical properties of these transparent junctions.

Another area of research, which is not yet explored completely, but has tremendous potential, is the thermoelectric properties of delafossite materials. Being a layered-structured material, delafossite films can become very good candidate for thermoelectric converters. If proper studies can be done on the thermoelectric properties of these types of superlattice materials, new horizon may open up in the field of thermoelectric converters.

Also keeping an eye in the tremendous progress in nanotechnology, fabrication and characterization of nanostructured p-TCO thin films may become an important field of work, because of new and interesting properties exhibited by these nanomaterials. Proper fabrication procedure to get reproducible nanomaterials is the most important future work. Also, in-depth studies of the photoluminescence properties of p-TCO nanoparticles will be another area of research, which is needed to be explored properly. Fabrication of nanostructured p-TCOs, coupled with the already existing and well-known materials of nanostructured n-TCOs, will give an added impetus in the field of “Invisible Electronics” for the fabrication of nanoactive devices, which can have high-efficient applications in the optoelectronic device technology.

Field-emission property of CuAlO_2 (as well as similar wide-bandgap TCO materials) thin films is a completely new area of research, which has tremendous opportunities. This material showed very low turn-on field comparable to most of the carbonaceous low-threshold field emitters like CNT, DLC, diamond, a:C, SiC nanorods, etc. So these types of wide-bandgap TCO materials may become promising alternative to the existing materials in the field of FED technology. But, proper emission mechanism in these materials is not very clear till date and very good scopes are there to properly investigate the emission mechanism so that the material properties can be tuned accordingly to get better field-emission properties of these films.

Also, recent study showed that p- CuAlO_2 can become a good candidate for ozone sensors. Zheng et al. [64] reported that CuAlO_2 has a selective and reversible response to ozone gas at room temperature. All existing commercial

semiconductor ozone sensors are of n-type [224–226]. This study demonstrated the feasibility of developing an inexpensive p-type transparent ozone sensor. Hence, transparent p–n junction ozone sensors may be fabricated using the p-CuAlO₂ and existing n-TCO such as In₂O₃.

Photocatalytic hydrogen evolution over delafossite CuAlO₂ is another interesting report published recently by Koriche et al. [65]. This group proposed a new photochemical system for water reduction based on p-CuAlO₂ and S²⁻ as hole scavenger. They have used coprecipitation method, a new synthetic route, to synthesis CuAlO₂, which increased the surface to volume ratio and delivered a highest H₂ production. This report is very interesting and shows newer applications of delafossite p-CuAlO₂ material.

Also, recently Kizaki et al. [66] proposed a material designing procedure to get CuAlO₂-based dilute magnetic semiconductors. Ab initio calculations showed that Fe- and Mn-doped CuAlO₂-based dilute magnetic semiconductors possess high-Curie-temperature ferromagnetic characteristics. Being a natural p-type transparent semiconductor without intentional doping, CuAlO₂ can easily be used for the host of dilute magnetic semiconductors. Also, most importantly, the delafossite structure of CuAlO₂ has the advantage of possessing two cation sites, Cu⁺¹ and Al⁺³ sites, for possible magnetic ion substitution. O–Cu–O dumbbell sites in delafossite CuAlO₂ can be partially replaced with magnetic ions. Due to this coordination, one can realize new ferromagnetic dilute magnetic semiconductors from the standpoint of the hybridization of orbitals between 3d orbitals with the impurities and 2p orbitals with the oxygen in CuAlO₂.

Regarding spinel p-TCO films, NiCo₂O₄ shows very good electrocatalytic behavior in many electrochemical processes such as hydrogen evolution, oxygen evolution, organic electrosynthesis, etc. [227, 228]. On the other hand, Reddy et al. [229] reported that nickel ferrite (NiFe₂O₄), a p-type semiconducting oxide with an inverse spinel structure, could be used as a gas sensor to selectively detect chlorine in air. Also recently, Saadi et al. [230] reported the photoassisted hydrogen evolution of p-type spinel CuM₂O₄ (M = Al/Cr/Fe/Mn/Co), indicating newer applications of these types of materials.

Therefore, it will not be an exaggeration to say that next decade will see the renaissance of spinel and delafossite, wide bandgap, p-TCO materials and various new, interesting and novel technological applications with these materials are on the verge of exploration.

Acknowledgments. The authors wish to thank Department of Science and Technology, Government of India, for financial support during the execution of the work reported in this chapter.

References

1. W.D. Westwood, *Sputter Deposition* (American Vacuum Society, New York, 2003), pp. 203–204
2. K. Wasa, M. Kitabatake, H. Adachi, *Thin Film Materials Technology* (William Andrew, Norwich, 2004) pp. 191–192
3. M. Ohring, *The Materials Science of Thin Films* (Academic, San Diego, 1992)
4. R.F. Bunshah, *Handbook of Deposition Technologies for Films and Coatings* (Noyes Publications, Park Ridge, 1994)
5. N. Tsuda, K. Nasu, A. Yanase, K. Siratori, *Electronic Conduction in Oxides* (Springer, Berlin Heidelberg New York, 1991)
6. C.N.R. Rao, B. Raveau, *Transition Metal Oxides* (Wiley-VCH, New York, 1998)
7. F.C. Phillips, *An Introduction to Crystallography*, 3rd edn. (Wiley, New York, 1963)
8. R.W.G. Wyckoff, *Crystal Structures*, 2nd edn. (Interscience, New York, 1963)
9. C. Kittel, *Introduction to Solid State Physics*, 3rd edn. (Wiley, New York, 1967)
10. N.W. Ashcroft, N.D. Mermin, *Solid State Physics* (Holt, Rinehart, and Winston, New York, 1976)
11. D.P. Norton, Mater. Sci. Eng. R **43**, 139 (2004)
12. R.D. Shannon, D.B. Rogers, C.T. Prewitt, Inorg. Chem. **10**, 713 (1971)
13. C.T. Prewitt, R.D. Shannon, D.B. Rogers, Inorg. Chem. **10**, 719 (1971)
14. D.B. Rogers, R.D. Shannon, C.T. Prewitt, J.L. Gillson, Inorg. Chem. **10**, 723 (1971)
15. A.N. Banerjee, K.K. Chattopadhyay, Prog. Cryst. Growth Charact. Mater. **50**, 52 (2005)
16. A.N. Banerjee, K.K. Chattopadhyay, in *P-Type Transparent Semiconducting Delafossite CuAlO_{2+x} Thin Film: Promising Material for Optoelectronic Devices and Field-Emission Displays in Materials Science Research Trends*, ed. by M.B. Olivante (Nova Science Publishers, New York, 2007) (in press)
17. R. Nagrajan, N. Duan, M.K. Jayaraj, J. Li, K.A. Vanaja, A. Yokochi, A. Draeseke, J. Tate, A.W. Sleight, Int. J. Inorg. Mater. **3**, 265 (2001)
18. M.A. Arillo, M.L. Lopez, E. Perez-Cappe, C. Pico, M.L. Veiga, Solid State Ionics **107**(3), 307 (1998)
19. V. Kahlenberg, C.S.J. Shaw, J.B. Parise, Am. Miner. **86**(11–12), 1477 (2001)
20. T. Yokoyama, Y. Abe, T. Meguro, K. Komeya, K. Kondo, S. Kaneko, T. Sasamoto, Jpn. J. Appl. Phys. **35**, 5775 (1996)
21. D.K. Kulkarni, C. Mande, J. Phys. D: Appl. Phys. **4**, 1218 (1971)
22. I. Okonska-Kozłowska, J. Kopyczok, H.D. Lutz, T. Stingl, Acta Cryst. C **49**, 1448 (1993)
23. A. Krimmel, Z. Seidov, G.G. Guseinov, A.I. Najafov, H.-A. Krug von Nidda, A. Loidl, D.M. Többens, J. Phys.: Condens. Matter **17**, 3611 (2005)
24. O. Morey, P. Goeriot, J. Eur. Ceram. Soc. **25**, 501 (2005)
25. K. Leinenweber, M. O’Keeffe, M. Somayazulu, H. Hubert, P.F. McMillan, G.H. Wolf, Chem.: Eur. J. **5**(10), 3076 (1999)
26. S.-D. Choi, B.-K. Min, Sens. Actuators B **77**, 330 (2001)
27. L.D. Young, T.J. Coutts, D.L. Williamson, Mater. Res. Soc. Symp. Proc. **666**, F3.8.1 (2001)
28. R.S. Liu, Y.C. Cheng, R. Gundakaram, L.Y. Jang, Mater. Res. Bull. **36**(7), 1479 (2001)

29. M. Wakaki, T. Ogawa, T. Arai, *Il Nuovo Cimento D* **2**(6), 1809 (1983)
30. S.-H. Wei, S.B. Zhang, *Phys. Rev. B* **63**, 045112.1 (2001)
31. F.S. Galasso, *Structure and Properties of Inorganic Solids* (Pergamon, New York, 1970)
32. D.C. Johnston, H. Prakash, W.H. Zachariasen, R. Viswanathan, *Mater. Res. Bull.* **8**, 777 (1973)
33. R.W. McCallum, D.C. Johnston, C.A. Luengo, M.B. Maples, *J. Low Temp. Phys.* **25**, 177 (1976)
34. E.W. Gorter, *Philips Res. Rep.* **9**, 295 (1954)
35. R.E. Vandenberghe, E. DeGrave, in *Mössbauer Spectroscopy Applied to Inorganic Chemistry*, vol. 3, ed. by G.J. Long, F. Grandjean (Plenum, New York, 1989), p. 59
36. S.H. Park, Y.-K. Sun, C.S. Yoon, C.-K. Kim, J. Prakash, *J. Mater. Chem.* **12**, 3827 (2002)
37. H.J. Kim, I.C. Song, J.H. Sim, H. Kim, D. Kim, Y.E. Ihm, W.K. Choo, *Mater. Sci. Forum* **449–452**, 509 (2004)
38. R.J. Hill, J.R. Craig, G.V. Gibbs, *Phys. Chem. Miner.* **4**, 317 (1979)
39. D.L. Anderson, *Science* **223**, 347 (1984)
40. Y.-M. Chiang, W.D. Kingery, *J. Am. Ceram. Soc.* **72**, 271 (1989)
41. Y.-M. Chiang, W.D. Kingery, *J. Am. Ceram. Soc.* **73**, 1153 (1990)
42. J. Nozik, *Phys. Rev. B* **6**, 453 (1972)
43. M. Labeau, V. Reboux, D. Dhahri, J.C. Joubert, *Thin Solid Films* **136**, 257 (1986)
44. N. Ueda, T. Omata, N. Hikuma, K. Ueda, H. Mizoquchi, T. Hashimoto, H. Kawazoe, *Appl. Phys. Lett.* **61**, 1954 (1992)
45. T.J. Coutts, X. Wu, W.P. Mulligan, J.M. Webb, *J. Electron. Mater.* **25**, 935 (1996)
46. J.C. Debsikdar, *J. Mater. Sci.* **20**, 4454 (1985)
47. H. Tanji, N. Kurihara, M. Yoshida, *J. Mater. Sci. Lett.* **13**, 1673 (1994)
48. H. Enoki, T. Nakayama, J. Echigoya, *Phys. Status Solidi A* **129**, 181 (1992)
49. X. Wu, T.J. Coutts, W.P. Mulligan, *J. Vac. Sci. Technol. A* **15**(3), 1057 (1997)
50. H. Kawazoe, K. Ueda, *J. Am. Ceram. Soc.* **82**(12), 3330 (1999)
51. X.Z. Wu, R. Ribelin, R.G. Dhere, D.S. Albin, T.A. Gessert, S. Asher, D.H. Levi, A. Mason, H.R. Moutinho, P. Sheldon, in *Proceedings of 28th IEEE PVSC*, Anchorage, Alaska, 17–22 September 2000, ed. by J. Benner
52. C.F. Windisch Jr., G.J. Exarhos, K.F. Ferris, M.H. Engelhard, D.C. Stewart, *Thin Solid Films* **398–399**, 45 (2001)
53. F. Windisch Jr., K.F. Ferris, G.J. Exarhos, *J. Vac. Sci. Technol. A* **19**(4), 1647 (2001)
54. M. Dekkers, G. Rijnders, D.H.A. Blank, *Appl. Phys. Lett.* **90**, 021903.1 (2007)
55. H. Mizoguchi, M. Hirano, S. Fujitsu, T. Takeuchi, K. Ueda, H. Hosono, *Appl. Phys. Lett.* **80**(7), 1207 (2002)
56. G. Thomas, *Nature* **389**, 907 (1997)
57. A.N. Banerjee, R. Maity, P.K. Ghosh, K.K. Chattopadhyay, *Thin Solid Films* **474**, 261 (2005)
58. M. Hasegawa, I. Inagawa, M. Tanaka, I. Shirotnani, H. Takei, *Solid State Commun.* **121**, 203 (2002)
59. K. Park, K.Y. Ko, W.-S. Seo, *Mater. Sci. Eng. B* **129**, 1 (2006)
60. K. Koumoto, H. Koduka, W.-S. Seo, *J. Mater. Chem.* **11**, 251 (2001)

61. K. Isawa, Y. Yaegashi, S. Ogota, M. Nagano, S. Sudo, K. Yamada, H. Yamauchi, *Phys. Rev. B* **57**(13), 7950 (1998)
62. M. Ohtaki, Y. Kubo, K. Eguchi, *Proc. XVII Int. Conf. Thermoelectr. (ICT 98)* **24**, 559 (1998)
63. A.N. Banerjee, K.K. Chattopadhyay, *Appl. Surf. Sci.* **225**, 243 (2004)
64. X.G. Zheng, K. Taniguchi, A. Takahashi, Y. Liu, C.N. Xu, *Appl. Phys. Lett.* **85**, 1728 (2004)
65. N. Koriche, A. Bouguelia, A. Aider, M. Trari, *Int. J. Hydrogen Energy* **30**, 693 (2005)
66. H. Kizaki, K. Sato, A. Yanase, H. Katayama-Yoshida, *Physica B* **376–377**, 812 (2006)
67. K. Badekar, *Ann. Phys. (Leipzig)* **22**, 749 (1907)
68. M. Lampert, *Sol. Energy Mater.* **6**, 1 (1981)
69. K.L. Chopra, S. Major, D.K. Pandya, *Thin Solid Films* **102**, 1 (1983)
70. I. Hamberg, C.G. Granqvist, *J. Appl. Phys.* **60**, R123 (1986)
71. L. Holland, *Vacuum Deposition of Thin Films* (Wiley, New York, 1958)
72. H. Cachet, A. Gamard, G. Campet, B. Jousseau, T. Toupance, *Thin Solid Films* **388**, 41 (2001)
73. R. Wendt, K. Ellmer, *Surf. Coat. Technol.* **93**, 27 (1997)
74. H.L. Hartnagel, A.L. Dawar, A.K. Jain, C. Jagadish, *Semiconducting Transparent Thin Films* (IOP Publishing, Bristol, 1995)
75. S. Ginley, C. Bright, *MRS Bull.* **25**, 15 (2000)
76. R.J. Cava, J.M. Philips, J. Kwo, G.A. Thomas, R.B. van Dover, S.A. Carter, J.J. Krajewski, W.F. Peck Jr., J.H. Marshall, D.H. Rapkin, *Appl. Phys. Lett.* **64**, 2071 (1994)
77. J.M. Philips, R.J. Cava, G.A. Thomas, S.A. Carter, J. Kwo, T. Siegrist, J.J. Krajewski, J.H. Marshall, W.F. Peck Jr., D.H. Rapkin, *Appl. Phys. Lett.* **67**, 2246 (1995)
78. J. Freeman, K.R. Poeppelmeier, T.O. Mason, R.P.H. Chang, T.J. Marks, *MRS Bull.* **25**, 45 (2000)
79. R.G. Gordon, *MRS Bull.*, **25**, 52 (2000)
80. B.G. Lewis, D.C. Paine, *MRS Bull.*, **25**, 22 (2000)
81. C.G. Granqvist, A. Azens, A. Hjelm, L. Kullman, G.A. Niklasson, D. Ronnow, M.S. Mattson, M. Veszeli, G. Vaivars, *Sol. Energy* **63**, 199 (1998)
82. R. Kammler, D.D. Edwards, B.J. Ingram, T.O. Mason, G.B. Palmer, A. Ambrosini, K.R. Poeppelmeier, in *Photovoltaics for the 21st Century*, Proceedings vol. 99-11, ed. by V.K. Kapur, R.D. McConnel, D. Carlson, G.P. Ceasan, A. Rohatgi (The Electrochemical Society, Pennington, 1999), pp. 68–70
83. S.H. Lee, K.H. Hwang, S.K. Joo, in *Electrochromic Materials (2nd International Symposium)*, Proceedings vol. 94-2, ed. by K.C. Ho, D.A. McArthur (The Electrochemical Society, Pennington, 1994), pp. 290–291
84. P.S. Lugg, S. Bommarito, J. Bailey, K. Budd, P. Cullen, K. Chen, L.C. Hardy, M. Nachbor, *Solid State Ionic Devices*, Proceedings vol. 99-13 (The Electrochemical Society, Pennington, 1999), pp. 284–286
85. Y. Nakato, K.I. Kai, K. Kawabe, *Sol. Energy Mater. Sol. Cells* **37**, 323 (1995)
86. T.T. Emons, J. Li, L.F. Nazar, *J. Am. Chem. Soc.* **124**, 8516 (2002)
87. M.G. Hutchins, G.D. McMeeking, *Biosensor Patent* 90,27,607.2 (1990)
88. Y. He, J. Kanicki, *Appl. Phys. Lett.* **76**, 661 (2000)

89. J.F. Wager, *Science* **300**, 1245 (2003)
90. C.M. Lampert, *Sol. Energy Mater. Sol. Cells* **76**, 489 (2003)
91. C. Grivas, S. Mallis, L. Boutsikaris, D.S. Gill, N.A. Vainos, P.J. Chandler, *Laser Phys.* **8**, 326 (1998)
92. K. Moschovis, E. Gagaoudakis, E. Chatzitheodoridis, G. Kiriakidis, S. Mailis, E. Tzamali, N.A. Vainos, H. Fritzsche, *Appl. Phys. A* **66**, 651 (1998)
93. S. Moller, C. Perlov, W. Jackson, C. Taussig, S.R. Forest, *Nature* **426**, 166 (2003)
94. R.A. Hayes, B.J. Feenstra, *Nature* **425**, 383 (2003)
95. R.L. Cornia, J.B. Fenn, H. Memarian, R. Ringer, *Proceedings of 41st Annual Technical Conference* (Society of Vacuum Coaters, Boston, 1998), p. 452
96. D.R. Cairns, R.P. Witte, D.K. Sparacin, S.M. Sachsman, D.C. Paine, G.P. Crawford, R. Newton, *Appl. Phys. Lett.* **76**, 1425 (2000)
97. N. Banerjee, C.K. Ghosh, K.K. Chattopadhyay, H. Minoura, A.K. Sarkar, A. Akiba, A. Kamiya, T. Endo, *Thin Solid Films* **496**, 112 (2006)
98. H. Seager, D.C. McIntyre, W.L. Warren, B.A. Tuttle, *Appl. Phys. Lett.* **68**, 2660 (1996)
99. M.W.J. Prince, K.O. Gross-Holtz, G. Muller, J.B. Cillessen, J.B. Giesbers, R.P. Weening, R.M. Wolf, *Appl. Phys. Lett.* **68**, 3650 (1996)
100. H. Kawazoe, M. Yasukawa, H. Hyodo, M. Kurita, H. Yanagi, H. Hosono, *Nature* **389**, 939 (1997)
101. H. Sato, T. Minami, S. Takata, T. Yamada, *Thin Solid Films* **236**, 27 (1993)
102. J.A.K. Tareen, A. Malecki, J.P. Doumerc, J.C. Launay, P. Dordor, M. Pouchard, P. Hagenmuller, *Mater. Res. Bull.* **19**, 989 (1984)
103. R.R. Owings, G.J. Exarhos, C.F. Windisch, P.H. Hollowaya, J.G. Wen, *Thin Solid Films* **483**, 175 (2005)
104. S. Narushima, H. Mizoguchi, H. Ohta, M. Hirano, K.-I. Shimizu, K. Ueda, T. Kamiya, H. Hosono, *Mater. Res. Soc. Symp. Proc.* **747**, V2.2.1 (2003)
105. R. Groth, *Phys. Status Solidi* **14**, 69 (1966)
106. H. Hahn, C.Z. Lorent, *Z. Anorg. Allg. Chem.* **279**, 281 (1955)
107. F.A. Benko, F.P. Koffyberg, *J. Phys. Chem. Solids* **45**, 57 (1984)
108. T. Ishiguro, A. Kitazawa, N. Mizutani, M. Kato, *J. Solid State Chem.* **40**, 170 (1981)
109. T. Ishiguro, N. Ishizawa, N. Mizutani, M. Kato, *J. Solid State Chem.* **41**, 132 (1982)
110. T. Ishiguro, N. Ishizawa, N. Mizutani, M. Kato, *Acta Cryst. B* **39**, 564 (1983)
111. K. Ueda, T. Hase, H. Yanagi, H. Kawazoe, H. Hosono, H. Ohta, M. Orita, M. Hirano, *J. Appl. Phys.* **89**, 1790 (2001)
112. H. Yanagi, T. Hase, S. Ibuki, K. Ueda, H. Hosono, *Appl. Phys. Lett.* **78**, 1583 (2001)
113. H. Yanagi, K. Ueda, H. Ohta, M. Orita, M. Hirano, H. Hosono, *Solid State Commun.* **121**, 15 (2001)
114. B.V. Kohler, M. Jansen, *Z. Anorg. Allg. Chem.* **543**, 73 (1986)
115. M. Shimode, M. Sasaki, K. Mukaida, *J. Solid State Chem.* **151**, 16 (2000)
116. H. Yanagi, S. Inoue, K. Ueda, H. Kawazoe, H. Hosono, N. Hamada, *J. Appl. Phys.* **88**, 4159 (2000)
117. J. Robertson, P.W. Peacock, M.D. Towler, R. Needs, *Thin Solid Films* **411**, 96 (2002)
118. B.J. Ingram, T.O. Mason, R. Asahi, K.T. Park, A.J. Freeman, *Phys. Rev. B* **64**, 155114.1 (2001)

119. J. Tate, M.K. Jayaraj, A.D. Draeseke, T. Ulbrich, A.W. Sleight, K.A. Vanaja, R. Nagrajan, J.F. Wager, R.L. Hoffman, *Thin Solid Films* **411**, 119 (2002)
120. N. Duan, A.W. Sleight, M.K. Jayaraj, J. Tate, *Appl. Phys. Lett.* **77**, 1325 (2000)
121. R. Nagrajan, A.D. Draeseke, A.W. Sleight, J. Tate, *J. Appl. Phys.* **89**, 8022 (2001)
122. K. Jayaraj, A.D. Draeseke, J. Tate, A.W. Sleight, *Thin Solid Films* **397**, 244 (2001)
123. F. Mattheiss, *Phys. Rev. B* **48**, 18300 (1993)
124. O. Crottaz, F. Kubel, H. Schmid, *J. Solid State Chem.* **122**, 247 (1996)
125. R. Nagrajan, S. Uma, M.K. Jayaraj, J. Tate, A.W. Sleight, *Solid State Sci.* **4**, 787 (2002)
126. E.M. Alkoy, P.J. Kelly, *Vacuum* **79**, 221 (2005)
127. T. Otabe, K. Ueda, A. Kudo, H. Hosono, H. Kawazoe, *Appl. Phys. Lett.* **72**, 1036 (1998)
128. R. Nagrajan, N. Duan, M.K. Jayaraj, J. Li, K.A. Vanaja, A. Yokochi, A. Draeseke, J. Tate, A.W. Sleight, *Int. J. Inorg. Mater.* **3**, 265 (2001)
129. Y.J. Shin, J.H. Kwak, S. Yoon, *Bull. Korean Chem. Soc.* **18**, 775 (1997)
130. J.-S. Kang, J.H. Kwak, Y.J. Shin, S.W. Han, K.H. Kim, B.I. Min, *Phys. Rev. B* **61**, 10682 (2000)
131. H.C. Kandpal, R. Seshadri, *Solid State Sci.* **4**, 1045 (2002)
132. H. Yanagi, S. Park, A.D. Draeseke, D.A. Keszler, J. Tate, *J. Solid State Chem.* **175**, 34 (2003)
133. L.I. Maissel, R. Glang, *Handbook of Thin Films Technology* (McGraw-Hill, New York, 1970)
134. D.B. Chrisey, G.K. Hubler, *Pulsed Laser Deposition of Thin Films* (Wiley-Interscience, New York, 1994)
135. K.L. Chopra, *Thin Film Phenomena* (McGraw-Hill, New York, 1969)
136. J.C. Anderson, *The Use of Thin Films in Physical Investigations* (Academic, New York, 1966)
137. H. Kawazoe, H. Yanagi, K. Ueda, H. Hosono, *MRS Bull.* **25**, 28 (2000)
138. R.E. Stauber, J.D. Perkins, P.A. Parilla, D.S. Ginley, *Electrochem. Solid State Lett.* **2**, 654 (1999)
139. B. Yang, Y.M. Lu, C. Neumann, A. Polity, C.Z. Wang, B.K. Meyer, *Mater. Res. Soc. Symp. Proc.* **905E**, 0905-DD05-09.1 (2006)
140. Y. Kakehi, S. Nakao, K. Satoh, T. Yotsuya, *Thin Solid Films* **445**, 294 (2003)
141. S. Gilliland, J.F. Sánchez-Royo, J. Pellicer-Porres, A. Segura, A. Muñoz, P. Rodríguez-Hernández, J. López-Solano, *Thin Solid Films* (2007), doi: 10.1016/j.tsf.2007.03.070
142. S. Gilliland, J. Pellicer-Porres, A. Segura, A. Munoz, P. Rodríguez-Hernández, D. Kim, M.S. Lee, T.Y. Kim, *Phys. Status Solidi B* **244**(1), 309 (2007)
143. A.N. Banerjee, S. Kundoo, K.K. Chattopadhyay, *Thin Solid Films* **440**, 5 (2003)
144. A.N. Banerjee, C.K. Ghosh, K.K. Chattopadhyay, *Sol. Energy Mater. Sol. Cells* **89**, 75 (2005)
145. J.H. Shy, B.H. Tseng, *J. Phys. Chem. Solids* **66**, 2123 (2005)
146. A.N. Banerjee, S. Nandy, C.K. Ghosh, K.K. Chattopadhyay, *Thin Solid Films* **515**(18), 7324 (2007)
147. H.K. Yoshida, T. Koyanagi, H. Funashima, H. Harima, A. Yanase, *Solid State Commun.* **126**, 135 (2003)

148. T. Koyanagi, H. Harima, A. Yanase, H.K. Yoshida, *J. Phys. Chem. Solids* **64**, 1443 (2003)
149. Y. Wang, H. Gong, F. Zhu, L. Liu, L. Huang, A.C.H. Huan, *Mater. Sci. Eng. B* **85**, 131 (2001)
150. Y. Wang, H. Gong, *Chem. Vapor Depos.* **6**, 285 (2000)
151. H. Gong, Y. Wang, Y. Luo, *Appl. Phys. Lett.* **76**, 3959 (2000)
152. D.-S. Kim, S.-Y. Choi, *Phys. Status Solidi A* **202**, R167 (2005)
153. P.K. Ghosh, A.N. Banerjee, K.K. Chattopadhyay (unpublished data)
154. K. Tonooka, K. Shimokawa, O. Nishimura, *Thin Solid Films* **411**, 129 (2002)
155. S. Gao, Y. Zhao, P. Gou, N. Chen, Y. Xie, *Nanotechnology* **14**, 538 (2003)
156. C. Bouzidi, H. Bouzouita, A. Timoumi, B. Rezig, *Mater. Sci. Eng. B* **118**, 259 (2005)
157. M. Ohashi, Y. Iida, H. Morikawa, *J. Am. Ceram. Soc.* **85**, 270 (2002)
158. H. Ong, H. Gong, *Thin Solid Films* **445**, 299 (2003)
159. F. Schubert, *Doping in III-V Semiconductors* (Cambridge University Press, Cambridge, 1993)
160. L.E. Brus, *J. Chem. Phys.* **80**, 4403 (1984)
161. N. Tsuboi, Y. Takahashi, S. Kobayashi, H. Shimizu, K. Kato, F. Kaneko, *J. Phys. Chem. Solids* **64**, 1671 (2003)
162. N. Tsuboi, Y. Itoh, J. Ogata, S. Kobayashi, H. Shimizu, K. Kato, F. Kaneko, *Jpn. J. Appl. Phys.* **46**, 351 (2007)
163. A.N. Banerjee, R. Maity, K.K. Chattopadhyay, *Mater. Lett.* **58**, 10 (2003)
164. A.N. Banerjee, C.K. Ghosh, S. Das, K.K. Chattopadhyay, *Physica B* **370**, 264 (2005)
165. S. Reddy, P.S. Reddy, S. Uthanna, G.M. Rao, *J. Mater. Sci. Mater. Electron.* **17**, 615 (2006)
166. H. Ohta, H. Mizoguchi, M. Hirano, S. Narushima, T. Kamiya, H. Hosono, *Appl. Phys. Lett.* **82**(5), 823 (2003)
167. S. Narushima, H. Mizoguchi, K.-I. Shimizu, K. Ueda, H. Ohta, M. Hirano, T. Kamiya, H. Hosono, *Adv. Mater.* **15**(17), 1409 (2003)
168. R.L. Hoffman, J.F. Wager, M.K. Jayaraj, J. Tate, *J. Appl. Phys.* **90**, 5763 (2001)
169. M.K. Jayaraj, A.D. Draeseke, J. Tate, R.L. Hoffman, J.F. Wager, *Mater. Res. Soc. Proc.* **666**, F4.1 (2001)
170. K. Tonooka, H. Bando, Y. Aiura, *Thin Solid Films* **445**, 327 (2003)
171. M.W.J. Prins, K.-O. Grosse-Holz, G. Müller, J.F.M. Cillessen, J.B. Giesbers, R.P. Weening, R.M. Wolf, *Appl. Phys. Lett.* **68**, 3650 (1996)
172. M.W.J. Prins, S.E. Zinnemers, J.F.M. Cillessen, J.B. Giesbers, *Appl. Phys. Lett.* **70**, 458 (1997)
173. R.L. Hoffman, B.J. Norris, J.F. Wager, *Appl. Phys. Lett.* **82**, 733 (2003)
174. S. Masuda, K. Kitamura, Y. Okumura, S. Miyatake, H. Tabata, T. Kawai, *J. Appl. Phys.* **93**, 1624 (2003)
175. F. Carcia, R.S. McLean, M.H. Reilly, G. Nunes Jr., *Appl. Phys. Lett.* **82**, 1117 (2003)
176. K. Nomura, H. Ohta, K. Ueda, T. Kamiya, M. Hirano, H. Hosono, *Science* **300**, 1269 (2003)
177. H. Ohta, K. Nomura, H. Hiramatsu, K. Ueda, T. Kamiya, M. Hirano, H. Hosono, *Solid State Electron.* **47**, 2261 (2003)
178. D. DeVault, *J. Chem. Educ.* **21**, 526 (1944)

179. J.C. Bailar Jr., H.J. Emeléus, Sir N. Roland, A.F. Trotman-Dickenson, *Comprehensive Inorganic Chemistry* (Pergamon, New York, 1973)
180. Y.K. Leung, A.K. Khan, J.F. Kos, F.P. Koffyberg, *Proceedings of National Conference on Solar Energy; Solar Energy Society of Canada*, Montreal, 1981, pp. 124–126
181. J.P. Dahl, A.C. Switendick, *J. Phys. Chem. Solids* **27**, 931 (1966)
182. M. Hayashi, K. Katsuki, *J. Phys. Soc. Jpn.* **5**, 380B (1950)
183. L. Kleinman, K. Mednick, *Phys. Rev. B* **21**, 1549 (1980)
184. P. Kofstad, *Nonstoichiometry, Diffusion, and Electrical Conductivity in Binary Metal Oxides* (Wiley-Interscience, New York, 1972)
185. J. Cava, W.F. Peck Jr., J.J. Krajewski, S.W. Cheong, H.Y. Hwang, *J. Mater. Res.* **9**, 314 (1994)
186. J. Cava, H.W. Zandbergen, A.P. Ramirez, H. Tagaki, C.T. Chien, J.J. Krajewski, W.F. Peck Jr., J.V. Waszczak, G. Meigs, R.S. Roth, L.F. Schneemeyer, *J. Solid State Chem.* **104**, 437 (1993)
187. M.K. Jayaraj, A. Draeseke, J. Tate, N. Duan, A.W. Sleight, *Proceedings of the MRS Workshop on Transparent Conductive Oxide*, Denever, CO, 19–20 June 2000
188. M.V. Lalić, J.M. Filho, A.W. Carbonari, R.N. Saxena, M. Morales, *J. Phys.: Condens. Matter* **14**, 5517 (2002)
189. M.V. Lalić, J.M. Filho, A.W. Carbonari, R.N. Saxena, *Solid State Commun.* **125**, 175 (2003)
190. M.V. Lalić, J. Mestnik-Filho, *Hyperfine Interact.* **158**, 89 (2004)
191. D.Y. Shahriari, A. Barnabè, T.O. Mason, K.R. Poeppelmeier, *Inorg. Chem.* **40**, 5734 (2001)
192. F.A. Benko, F.P. Koffyberg, *J. Phys. Chem. Solids* **48**, 431 (1987)
193. A. Kudo, H. Yanagi, K. Ueda, H. Hosono, H. Kawazoe, Y. Yano, *Appl. Phys. Lett.* **75**, 2851 (1999)
194. A. Kudo, H. Yanagi, H. Hosono, H. Kawazoe, *Appl. Phys. Lett.* **73**, 220 (1998)
195. K. Ueda, S. Inoue, S. Hirose, H. Kawazoe, H. Hosono, *Appl. Phys. Lett.* **77**, 2701 (2000)
196. H. Hiramatsu, K. Ueda, H. Ohta, M. Orita, M. Hirano, H. Hosono, *Thin Solid Films* **411**, 125 (2002)
197. T. Minami, K. Shimokawa, T. Miyata, *J. Vac. Sci. Technol. A* **16**, 1218 (1998)
198. H. Sato, T. Minami, S. Takata, T. Yamada, *Thin Solid Films* **236**, 27 (1993)
199. J. Wang, G. Du, B. Zhao, X. Yang, Y. Zhang, Y. Ma, D. Liu, Y. Chang, H. Wang, H. Yang, S. Yang, *J. Cryst. Growth* **255**, 293 (2003)
200. D.C. Look, D.C. Reynolds, C.W. Litton, R.L. Jones, D.B. Eason, G. Cantwell, *Appl. Phys. Lett.* **81**, 1830 (2002)
201. B.M.A. Ashrafi, I. Suemune, H. Kumano, S. Tanaka, *Jpn. J. Appl. Phys.* **41**, L1281 (2002)
202. T. Yamamoto, H.K. Yoshida, *Jpn. J. Appl. Phys.* **38**, L166 (1999)
203. M. Joseph, H. Tabata, T. Kawai, *Jpn. J. Appl. Phys.* **38**, L1205 (1999)
204. H. Hiramatsu, K. Ueda, H. Ohta, M. Hirano, T. Kamiya, H. Hosono, *Appl. Phys. Lett.* **82**, 1048 (2003)
205. J. Robertson, *Diam. Relat. Mater.* **5**, 797 (1996)
206. K. Hirakuri, T. Yokoyama, H. Enomoto, N. Mutsukura, G. Friedbacher, *J. Appl. Phys.* **89**, 8253 (2001)
207. Power Diffraction File, Joint Committee on Powder Diffraction Standards (ASTM, Philadelphia, 1967), Card # 35 1401

208. D. Cullity, *Elements of X-ray diffraction* (Addison-Wesley, Reading, 1978)
209. J.I. Pankove, *Optical Processes in Semiconductors* (Prentice-Hall, Englewood Cliffs, 1971)
210. T.S. Moss, *Optical Properties of Semiconductors* (Butterworths, London, 1959)
211. F. Demichelis, G. Kaniadakis, A. Tagliaferro, E. Tresso, *Appl. Optics* **26**, 1737 (1987)
212. J. Szczyrbowski, K. Schmalzbauer, H. Hoffmann, *Thin Solid Films* **137**, 169 (1986)
213. K. Gurumurugan, D. Mangalaraj, S.K. Narayandass, *Thin Solid Films* **251**, 7 (1994)
214. J. Bardeen, F.J. Blatt, L.H. Hall, *Proceedings of Atlantic City Photoconductivity Conference* (Wiley/Chapman and Hall, New York, 1956)
215. D. Hicks, M.S. Dresselhaus, *Phys. Rev. B* **47**, 12727 (1993)
216. L.D. Hicks, T.C. Herman, M.S. Dresselhaus, *Appl. Phys. Lett.* **63**, 3230 (1993)
217. P.J. Lin-Chung, T.L. Reinecke, *Phys. Rev. B* **51**, 13244 (1995)
218. D.A. Broido, T.L. Reinecke, *Phys. Rev. B* **51**, 13797 (1995)
219. I. Terasaki, Y. Sasago, K. Uchinokura, *Phys. Rev. B* **56**, R12685 (1997)
220. Y. Masuda, M. Ohta, W.S. Seo, W. Pitschke, K. Koumoto, *J. Solid State Chem.* **150**, 221 (2000)
221. Y. Wang, N.S. Rogado, R.J. Cava, N.P. Ong, *Nature* **423**, 425 (2003)
222. R.K. Willardson, A.C. Beer, *Semiconductors and Semimetals*, vol. 8 (Academic, New York, 1971)
223. T. Kurotori, S. Sugihara, *Mater. Trans.* **46**, 1462 (2005)
224. D. Sauter, U. Weimar, G. Noetzel, J. Mitrovics, W. Gopel, *Sens. Actuators B* **69**, 1 (2000)
225. S.-R. Kim, H.-K. Hong, C.H. Kwon, D.H. Yun, K. Lee, Y.K. Sung, *Sens. Actuators B* **66**, 59 (2000)
226. E. Gagaoudakis, M. Bender, E. Douloufakis, N. Katsuarakis, E. Natsakou, V. Cimalla, G. Kiriakidis, *Sens. Actuators B* **80**, 155 (2001)
227. C. Bo, J.-B. Li, Y.-S. Han, J.-H. Dai, *Mater. Lett.* **58**, 1415 (2004)
228. C. Bo, X. Yang, J. Li, N. Wang, *Key. Eng. Mater.* **280–283**, 561 (2005)
229. C.V.G. Reddy, S.V. Manorama, V.J. Roa, *Sens. Actuators* **B55**, 90 (1999)
230. S. Saadi, A. Bougelia, M. Trari, *Renew. Energy* **31**, 2245 (2006)